KeAi
CHINESE ROOTS
GLOBAL IMPACT

Contents lists available at ScienceDirect

Petroleum Science

journal homepage: www.keaipublishing.com/en/journals/petroleum-science



Original Paper

Simultaneous seismic inversion of effective stress parameter, fluid bulk modulus, and fracture density in TTI media



Yun Zhao ^{a, b}, Xiao-Tao Wen ^{a, b, *}, Chun-Lan Xie ^{a, b}, Bo Li ^{a, b}, Chen-Long Li ^{a, c}, Xiao Pan ^{a, b}, Xi-Yan Zhou ^{a, b}

- ^a Key Laboratory of Earth Exploration and Information Techniques, Ministry of Education, Chengdu University of Technology, Chengdu, 610059, Sichuan, China
- ^b College of Geophysics, Chengdu University of Technology, Chengdu, 610059, Sichuan, China
- ^c South Branch of SINOPEC Petroleum Engineering Geophysical Co., Ltd, Chengdu, 610041, Sichuan, China

ARTICLE INFO

Article history:
Received 2 August 2024
Received in revised form
30 October 2024
Accepted 1 April 2025
Available online 2 April 2025

Edited by Meng-Jiao Zhou

Keywords: Shale gas Effective stress parameter Fracture density TTI Anisotropic inversion

ABSTRACT

Predictions of fluid distribution, stress field, and natural fracture are essential for exploiting unconventional shale gas reservoirs. Given the high likelihood of tilted fractures in subsurface formations, this study focuses on simultaneous seismic inversion to estimate fluid bulk modulus, effective stress parameter, and fracture density in the tilted transversely isotropic (TTI) medium. In this article, a novel PP-wave reflection coefficient approximation equation is first derived based on the constructed TTI stiffness matrix incorporating fracture density, effective stress parameter, and fluid bulk modulus. The high accuracy of the proposed equation has been demonstrated using an anisotropic two-layer model. Furthermore, a stepwise seismic inversion strategy with the L_P quasi-norm sparsity constraint is implemented to obtain the anisotropic and isotropic parameters. Three synthetic model tests with varying signal-to-noise ratios (SNRs) confirm the method's feasibility and noise robustness. Ultimately, the proposed method is applied to a 3D fractured shale gas reservoir in the Sichuan Basin, China. The results have effectively characterized shale gas distribution, stress fields, and tilted natural fractures, with validation from geological structures, well logs, and microseismic events. These findings can provide valuable guidance for hydraulic fracturing development, enabling more reliable predictions of reservoir heterogeneity and completion quality.

© 2025 The Authors. Publishing services by Elsevier B.V. on behalf of KeAi Communications Co. Ltd. This is an open access article under the CC BY-NC-ND license (http://creativecommons.org/licenses/by-nc-nd/

4.0/).

1. Introduction

To effectively guide hydraulic fracturing (Hubbert and Willis, 1957; Wen et al., 2024) in unconventional shale reservoirs with ultralow porosity and permeability, fluid identification, stress prediction, and natural fracture detection play essential geophysical roles in shale gas reservoir modification (Zhang et al., 2018; Li et al., 2021, 2022a; Zhao et al., 2024). Geophysical parameter inversion based on offset vector tile (OVT)-domain seismic data provides valuable reference information for shale gas development.

Hydrocarbon fluid identification is a prerequisite for optimal well placement and delineation of productive zones in shale gas reservoirs (Ma et al., 2023; Yin and Zhang, 2014). Extensive

methodologies for fluid identification have been developed in both the time and frequency domains. For the time-domain approaches, conventional fluid indicators constructed with elasticity parameters have been widely employed to identify fluids in prestacked seismic inversion, including the product of Lamé constant and rock density $(\lambda \rho - \mu \rho - \lambda \mu)$ (Goodway et al., 1997), the P- to S-wave velocity ratio (Ding et al., 2019; Uyanik, 2010), and Russell fluid factor (Russell et al., 2011). Nevertheless, seismic anisotropy induced by fluidsaturated fractured rocks necessitates more advanced treatments. Under the weak anisotropy (WA) theory, considering that fracture normal weakness is sensitive to fluids and fracture tangential weakness is fluid-independent, the ratio of normal to tangential fracture flexibilities (K_N/K_T) (Schoenberg and Sayers, 1995) has been widely used for fluid identification. Recent advancements have integrated fracture parameters into fluid indicators, exemplified by the anisotropic fluid factor (FF), expressed in terms of fracture

E-mail address: wenxiaotao@cdut.cn (X.-T. Wen).

^{*} Corresponding author.

weakness and dry normal weakness as $1-\delta_T/\delta_N^{dry}(\text{Xue et al., 2017})$, the coupled anisotropic fluid indicator (δ_f) (Pan et al., 2020a) and the fracture gas indication factor (GFI) (Zhao et al., 2024). Despite their utility, these fluid indicators formulated as empirical parameter combinations remain susceptible to interference from porosity and fracture parameters. To address this limitation, direct seismic inversion of fluid bulk modulus decoupled from matrix and fracture effects has emerged as a more robust alternative (Yin and Zhang, 2014; Li et al., 2021, 2022a). In this study, we achieve fluid bulk modulus decoupling in the tilted transversely isotropic (TTI) medium with fractures by integrating anisotropic Gassmann fluid substitution equation with the linear slip model (Schoenberg and Douma, 1988).

Investigating in-situ stress can enhance hydraulic fracturing performance (Lin et al., 2022; Seto et al., 1999; Zhang et al., 2018; Yin et al., 2018). It is acknowledged that the in-situ stress consists of three principal stress components: vertical principal stress, and the maximum and minimum horizontal principal stresses. Current methods for in-situ stress assessment encompass three primary approaches: field surveys (Nakamura et al., 1997), well-log-based geomechanical modeling (Nikolaevskiy and Economides, 2000), and seismic predictions (Gray et al., 2010). For seismic-based stress inversion, anisotropic fracture-equivalent medium modeling is indispensable. Early studies approximated shale reservoirs as vertical transversely isotropic (VTI) media for stress estimation (Zhang et al., 2015). To simplify prediction, the low differential horizontal stress ratio (DHSR) was utilized to characterize the rock susceptibility to complex fracture network generation under external loading (Gray et al., 2012). Subsequent advances include the following: Ma et al. (2017, 2018) proposed the orthotropic DHSR (ODHSR) to assess stress in orthotropic anisotropic (OA) media, correlating stress-strain relationships with fracturing potential; Pan and Liu (2024) derived anisotropic parameters and stress prediction considering stress factors in the VTI medium; Li et al. (2022a, 2021) derived the linearized PP-wave reflection coefficient with vertical effective stress-sensitive parameter in the horizontal transversely isotropic (HTI) medium; Li et al. (2022b) derived the PP-wave reflection coefficient in the OA medium incorporating stress-related parameters. Despite these advancements, stress characterization in the TTI medium with tilted natural fractures remains insufficiently studied. This study focuses on the preliminary method of inverting stress parameters from the OVT domain seismic data and deriving the PP-wave reflection coefficient incorporating the relevant stress parameters in the TTI medium.

Furthermore, natural fractures in hydrocarbon reservoirs play a critical role in governing fluid migration and storage capacity, directly influencing production efficiency and ultimate recovery (Sayers and Dean, 2001; Zhang et al., 2020; Guo et al., 2022a). Hydraulic stimulation can activate these fractures, creating interconnected networks that enhance hydrocarbon mobility. Anisotropic seismic fracture characterization primarily focuses on two critical parameter categories: fracture weaknesses (Schoenberg and Douma, 1988; Bakulin et al., 2000a) and anisotropy parameters (Thomsen, 1986), both of which are crucial for assessing fracture intensity (Lin et al., 2022; Guo et al., 2022b). Subsurface fractures with dominant orientations induce seismic anisotropy, commonly modeled through fracture equivalent media, including HTI medium with the horizontal axis of symmetry (Bakulin et al., 2000a), layered vertical transversely isotropic (VTI) medium with a vertical axis of symmetry, orthorhombic anisotropic (OA) medium (Bakulin et al., 2000b), and tilted transversely isotropic (TTI) medium

(Bakulin et al., 2000c). Born scattering theory and the stationary phase method provide the foundation for linearizing the PP-wave reflection coefficient (Shaw and Sen, 2004, 2006). These linearized PP-wave reflection coefficients enable the direct extraction of fracture parameters from azimuthal seismic data in various anisotropic media, including the standard HTI medium (Ruger, 1998; Chen et al., 2014, 2017; Pan et al., 2017), OA medium (Li et al., 2022b: Pan et al., 2018a, 2018b: Pšenčík and Martins, 2001), TTI medium (Ma et al., 2022; Pan et al., 2020b; Chen et al., 2020a). The linear PP-wave reflection coefficient derived for the TTI medium embedded in a VTI background is more suitable for characterizing shale fractures when the tilted fractures are developed in shale (Qin et al., 2022). To address this limitation, we propose a novel PP-wave reflectivity that explicitly integrates fracture density within the dual-phase medium framework, enabling the direct inversion of fracture density from azimuthal seismic data.

This article provides the simultaneous seismic inversion method for fluid bulk modulus, effective stress parameter, and fracture density in TTI media, addressing fluid identification, stress assessment, and natural fracture prediction. To begin with, we establish the stiffness matrix of saturated anisotropic TTI media based on the quantitative relationship between dry fracture weaknesses and fracture density. The skeleton gain function (Han and Batzle, 2003; Yin and Zhang, 2014) is introduced to decouple fluid bulk modulus from porosity via the effective stress parameter. Based on the acquired TTI stiffnesses, incorporating the fracture density and the effective stress parameter, the approximate stiffness perturbations are deduced under the assumption of small perturbations in the elasticity parameters across the interfaces. These perturbations are then utilized to obtain the linearized PP-wave reflection coefficient equation by Born scattering theory (Shaw and Sen, 2004, 2006), realizing the direct seismic inversion of fluid bulk modulus, effective stress parameter, and fracture density in the TTI medium. The high accuracy of equation is validated from azimuths, incidence angles, and fracture inclination angles. A stepwise inversion strategy (Chen et al., 2020a; Guo et al., 2022c; Zhao et al., 2024) based on the L_P quasi-norm sparsity constraint (Zhao et al., 2023) is applied to decouple these parameters from the OVT domain seismic data, ignoring azimuthal wavelet differences. Three synthetic models with varying SNRs confirm the method's feasibility and noise robustness. Eventually, the method has been applied to a fractured shale gas reservoir in the Sichuan Basin, China, and the inversion results exhibit satisfactory agreement with well logs, geological structures, and microseismic events, demonstrating its reliability for shale gas development.

2. Methodology

2.1. Linearized PP-wave reflection coefficient equation

Tilted fractures are commonly found in the subsurface, and the anisotropy induced by fracture inclination cannot be neglected. Based on the fluid substitution equation, the stiffness matrix of saturated rock can be expressed as the sum of the stiffness matrix of the dry rock skeleton and the anisotropic fluid component (Brown and Korringa, 1975; Mavko et al., 2009). The Bond transformation theory (Winterstein, 1990) for parallel fractures accounts for fracture inclination. Assuming small fracture weakness parameters, the stiffness matrix \mathbf{C}^{TII} of anisotropic saturated rock is given by (Ma et al., 2022, 2023):

$$\mathbf{C}^{\text{TTI}} = \begin{pmatrix} C_{11}^{\text{sat}} & C_{12}^{\text{sat}} & C_{13}^{\text{sat}} & 0 & C_{15}^{\text{sat}} & 0 \\ C_{12}^{\text{sat}} & C_{22}^{\text{sat}} & C_{23}^{\text{sat}} & 0 & C_{25}^{\text{sat}} & 0 \\ C_{13}^{\text{sat}} & C_{23}^{\text{sat}} & C_{23}^{\text{sat}} & 0 & C_{25}^{\text{sat}} & 0 \\ C_{13}^{\text{sat}} & C_{23}^{\text{sat}} & C_{33}^{\text{sat}} & 0 & C_{35}^{\text{sat}} & 0 \\ 0 & 0 & 0 & C_{44}^{\text{sat}} & 0 & C_{46}^{\text{sat}} \\ C_{15}^{\text{sat}} & C_{25}^{\text{sat}} & C_{35}^{\text{sat}} & 0 & C_{55}^{\text{sat}} & 0 \\ 0 & 0 & 0 & C_{46}^{\text{sat}} & 0 & C_{56}^{\text{sat}} \end{pmatrix}_{6 \times 6}$$

$$(1)$$

where the specific expressions for $C_{ij}^{\rm sat}$ are detailed in Appendix A, the subscript "ij" denotes the element position, and the superscript "sat" represents fluid-saturated rock. Based on fracture weaknesses (Schoenberg and Douma, 1988; Bakulin et al., 2000a) incorporating fracture density, fluid bulk modulus, and fracture aspect ratio, the normal and tangential fracture weaknesses of dry fractures can be rigorously expressed as

$$\delta_{N}^{dry} = \Gamma_{N} e^{TTI}$$
 and $\delta_{T}^{dry} = \Gamma_{T} e^{TTI}$ (2)

in which

$$\Gamma_{\text{N}} = \frac{4}{3g_{\text{d}}(1 - g_{\text{d}})}$$
 and $\Gamma_{\text{T}} = \frac{16}{3(3 - 2g_{\text{d}})}$ (3)

where $\delta_{\rm N}^{\rm dry}$ and $\delta_{\rm T}^{\rm dry}$ represent the normal and tangential weaknesses of dry fractures, respectively, $e^{\rm TII}$ denotes the fracture density in the TTI medium, the superscript "dry" indicates the dry rock skeleton, $\Gamma_{\rm N}$ and $\Gamma_{\rm T}$ denote the weighting coefficients relating fracture density to normal and tangential weaknesses, respectively, and the parameter $g_{\rm d}$ is the P- to S-wave velocity ratio in the dry rock skeleton, calculated as the dry P-wave modulus $M_{\rm d}$ divided by the shear modulus $\mu_{\rm b}$. Given that the shear modulus of the fluid is zero, the saturated and dry rock skeletons share the same shear modulus.

In the TTI medium, as illustrated in Fig. 1, rock porosity can be expressed as the sum of fracture porosity and background (unfractured) porosity. Compared to background porosity, fracture porosity approaches zero in the thin coin-shaped fracture model when the fracture aspect ratio tends to zero, etc., $\phi_f \rightarrow 0$, and then $\phi \approx \phi_p$. Numerous experimental studies have demonstrated that rock porosity is negatively correlated with vertical effective stress, and this quantitative relationship was given as (Athy, 1930; Rubey and Hubbert, 1959; Flemings et al., 2002; Dutta, 2002; Long et al., 2011; Chen et al., 2020b):

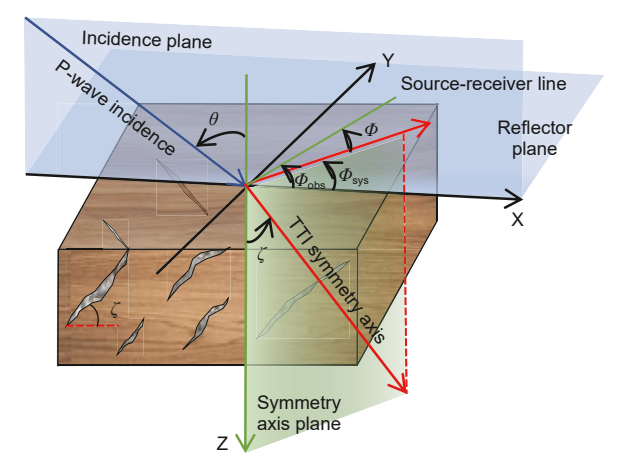


Fig. 1. Schematic of the TTI medium harboring a group of tilted fractures.

$$\phi_{\rm p} = \phi_0 \exp(-\beta \sigma_{\rm V}) \tag{4}$$

where ϕ_0 and σ_V represent the initial empirical porosity and the vertical effective stress of rock, respectively. Specifically, we symbolize the term $\sigma_E = \exp(-\beta\sigma_V)$ as the effective stress parameter, the symbol "exp" represents the exponential function, and β denotes the empirical effective stress coefficient related to the solidification of rocks (Kauerauf and Hantschel, 2009):

$$\sigma_{V} = P_{Z} - P_{p} \tag{5}$$

where P_Z denotes the overburden strata or vertical stress, and P_P denotes the pore pressure generated by fluids in fractures and pores acting on the formation. Therefore, the effective stress parameter σ_E is generally negatively correlated with the vertical effective stress σ_V and positively correlated with the pore pressure P_P .

The widely used gain function can be applied to decouple the background unfractured porosity term from the fluid term, establishing a quantitative relationship between the dry rock skeleton and fluid substitution (Han and Batzle, 2003; Yin and Zhang, 2014). This relationship is expressed as follows:

$$G_{\rm n}\left(\phi_{\rm p}\right) = \left(1 - K_{\rm d}/K_{\rm m}\right)^2/\phi_{\rm p} = \phi_{\rm p}/\phi_{\rm c}^2 = \sigma_{\rm E}\phi_{\rm 0}/\phi_{\rm c}^2$$
 (6)

where $G_{\rm n}(\phi_{\rm p})$ denotes the gain function used to characterize the dry rock skeleton, the parameters $K_{\rm d}$ and $K_{\rm m}$ represent the bulk moduli of the dry rock skeleton and the mineral matrix, respectively, and $\phi_{\rm c}$ represents the critical porosity.

To directly extract fracture density and the effective stress parameter from seismic data, Eqs. (2), (3) and (6) are substituted into Eq. (1). Consequently, the stiffnesses of the saturated anisotropic TTI medium can be expressed as

$$C_{11}^{\text{sat}} \approx M_{\text{d}} - M_{\text{d}} \left[\left(1 - 2g_{\text{d}} \cos^2 \zeta \right)^2 \Gamma_{\text{N}} + g_{\text{d}} (\sin 2\zeta)^2 \Gamma_{\text{T}} \right] e^{\text{TTI}}$$

$$+ \sigma_{\text{E}} \phi_0 K_{\text{f}} / \phi_{\text{c}}^2$$
(7)

$$C_{12}^{\text{sat}} \approx \lambda_{\text{d}} + \Gamma_{\text{N}} M_{\text{d}} \chi_{\text{d}} \left(2g_{\text{d}} \cos^2 \zeta - 1 \right) e^{\text{TTI}} + \sigma_{\text{E}} \phi_0 K_{\text{f}} / \phi_{\text{c}}^2$$
 (8)

$$\begin{split} C_{13}^{sat} \approx \lambda_{\rm d} - M_{\rm d} \Big\{ \Big[1 + g_{\rm d}^{\ 2} (\sin 2\zeta)^2 - 2g_{\rm d} \Big] \Gamma_{\rm N} - g_{\rm d} (\sin 2\zeta)^2 \Gamma_{\rm T} \Big\} e^{\rm TTI} \\ + \sigma_{\rm E} \phi_0 K_{\rm f} \left/ \phi_{\rm c}^{\ 2} \right. \end{split}$$

(9)

$$C_{22}^{\text{sat}} \approx M_{\text{d}} \left[1 - \Gamma_{\text{N}} \chi_{\text{d}}^2 e^{\text{TTI}} \right] + \sigma_{\text{E}} \phi_0 K_{\text{f}} / \phi_{\text{c}}^2$$
 (10)

$$C_{23}^{\rm sat} \approx \lambda_{\rm d} - \Gamma_{\rm N} \lambda_{\rm d} \left[1 - 2g_{\rm d} \sin^2 \zeta \right] e^{\rm TTI} + \sigma_{\rm E} \phi_0 K_{\rm f} / \phi_{\rm c}^2 \tag{11}$$

$$C_{25}^{\text{sat}} \approx \mu_{\text{b}} \chi_{\text{d}} \Gamma_{\text{N}} \sin 2\zeta e^{\text{TTI}}$$
 (12)

$$\begin{split} C_{33}^{\text{sat}} &\approx M_{\text{d}} - M_{\text{d}} \bigg[\Gamma_{\text{N}} \Big(1 - 2g_{\text{d}} \sin^2 \zeta \Big)^2 + \Gamma_{\text{T}} g_{\text{d}} \sin^2 2\zeta \bigg] e^{\text{TTI}} \\ &+ \sigma_{\text{E}} \phi_0 K_{\text{f}} / \phi_{\text{c}}^2 \end{split} \tag{13}$$

$$C_{15}^{\text{sat}} \approx \mu_{\text{b}} \left[\left(1 - 2g_{\text{d}} \cos^2 \zeta \right) \Gamma_{\text{N}} + \cos 2\zeta \ \Gamma_{\text{T}} \right] \sin 2\zeta \ e^{\text{TTI}}$$
 (14)

$$C_{35}^{\text{sat}} \approx \mu_{\text{b}} \left[\left(1 - 2g_{\text{d}} \sin^2 \zeta \right) \Gamma_{\text{N}} - \cos 2\zeta \Gamma_{\text{T}} \right] \sin 2\zeta \ e^{\text{TTI}}$$
 (15)

$$C_{AA}^{\text{sat}} = \mu_{\text{b}} - \Gamma_{\text{T}} \mu_{\text{b}} \cos^2 \zeta e^{\text{TTI}}$$
 (16)

$$C_{46}^{\text{sat}} = \frac{1}{2} \Gamma_{\text{T}} \mu_{\text{b}} \sin 2\zeta e^{\text{TTI}}$$

$$\tag{17}$$

$$C_{55}^{\text{sat}} \approx \mu_{\text{b}} - \mu_{\text{b}} \left[g_{\text{d}} (\sin 2\zeta)^2 \Gamma_{\text{N}} + (\cos 2\zeta)^2 \Gamma_{\text{T}} \right] e^{\text{TTI}}$$
 (18)

$$C_{66}^{\text{sat}} = \mu_{\text{b}} - \Gamma_{\text{T}} \mu_{\text{b}} \sin^2 \zeta \, e^{\text{TTI}} \tag{19}$$

where ζ represents the fracture inclination angle, as shown in Fig. 1, and $\chi_{\rm d}=\lambda_{\rm d}/M_{\rm d}$, in which $\lambda_{\rm d}$ is the first Lamé coefficient of the dry rock skeleton. Under the assumptions of weak anisotropy (WA) and small perturbations or weak contrasts in background elasticity moduli across the interface, fracture density is generally smaller than 0.1. Consequently, terms proportional to $\Delta M_{\rm d} e^{\rm TTI}$, $\Delta \mu_{\rm b} e^{\rm TTI}$, and $\Delta \lambda_{\rm d} e^{\rm TTI}$ in Eqs. (7)–(19) are negligible, simplifying the stiffness expressions for the subsequent linearization of the PP-wave reflection coefficient. The perturbations of the stiffness coefficients in the saturated TTI medium are then given as

$$\begin{split} \Delta C_{11}^{\text{sat}} &\approx \Delta M_{\text{d}} - M_{\text{d}} \bigg[\Big(1 - 2 g_{\text{d}} \, \cos^2 \zeta \Big)^2 \Gamma_{\text{N}} + g_{\text{d}} (\sin 2 \zeta)^2 \Gamma_{\text{T}} \bigg] \Delta e^{\text{TTI}} \\ &+ \Big(\sigma_{\text{E}} \Delta K_{\text{f}} + K_{\text{f}} \Delta \sigma_{\text{E}} \Big) \phi_0 \, \big/ \, \phi_{\text{c}}^2 \end{split}$$

$$\Delta C_{12}^{\text{sat}} \approx \Delta \lambda_{\text{d}} + \Gamma_{\text{N}} M_{\text{d}} (1 - 2g_{\text{d}}) \left(2g_{\text{d}} \cos^2 \zeta - 1 \right) \Delta e^{\text{TTI}} + \left(\sigma_{\text{E}} \Delta K_{\text{f}} + K_{\text{f}} \Delta \sigma_{\text{E}} \right) \phi_0 / \phi_c^2$$
(21)

$$\begin{split} \Delta C_{13}^{sat} &\approx \Delta \lambda_{\rm d} - M_{\rm d} \left\{ \left[1 + g_{\rm d}^{2} (\sin 2\zeta)^{2} - 2g_{\rm d} \right] \Gamma_{\rm N} - g_{\rm d} (\sin 2\zeta)^{2} \Gamma_{\rm T} \right\} \\ &\Delta e^{\rm TTI} + \left(\sigma_{\rm E} \Delta K_{\rm f} + K_{\rm f} \Delta \sigma_{\rm E} \right) \phi_{\rm 0} / \phi_{\rm c}^{2} \end{split} \tag{22}$$

$$\begin{split} \Delta C_{22}^{\text{sat}} &\approx \Delta M_{\text{d}} - \Gamma_{\text{N}} M_{\text{d}} (1 - 2g_{\text{d}})^2 \Delta e^{\text{TTI}} \\ &+ \left(\sigma_{\text{E}} \Delta K_{\text{f}} + K_{\text{f}} \Delta \sigma_{\text{E}} \right) \phi_0 / \phi_c^2 \end{split} \tag{23}$$

$$\begin{split} \Delta C_{23}^{sat} &\approx \Delta \lambda_{d} - \Gamma_{N} \lambda_{d} \left[1 - 2 g_{d} \, \sin^{2} \zeta \right] \Delta e^{TTI} \\ &+ \left(\sigma_{E} \Delta K_{f} + K_{f} \Delta \sigma_{E} \right) \phi_{0} \, / \, \phi_{c}^{2} \end{split} \tag{24}$$

$$\Delta C_{33}^{\text{sat}} \approx \Delta M_{\text{d}} - M_{\text{d}} \left[\Gamma_{\text{N}} \left(1 - 2g_{\text{d}} \sin^2 \zeta \right)^2 + \Gamma_{\text{T}} g_{\text{d}} \sin^2 2\zeta \right] \Delta e^{\text{TTI}}$$

$$+ \left(\sigma_{\text{E}} \Delta K_{\text{f}} + K_{\text{f}} \Delta \sigma_{\text{E}} \right) \phi_0 / \phi_{\text{c}}^2$$
(25)

$$\Delta C_{15}^{\text{sat}} \approx \mu_{\text{b}} \left[\left(1 - 2g_{\text{d}} \cos^2 \zeta \right) \Gamma_{\text{N}} + \cos 2\zeta \Gamma_{\text{T}} \right] \sin 2\zeta \Delta e^{\text{TTI}}$$
 (26)

$$\Delta C_{25}^{\text{sat}} \approx \mu_{\text{b}} (1 - 2g_{\text{d}}) \Gamma_{\text{N}} \sin 2\zeta \, \Delta e^{\text{TTI}}$$
(27)

$$\Delta C_{35}^{\text{sat}} \approx \mu_{\text{b}} \left[\left(1 - 2g_{\text{d}} \sin^2 \zeta \right) \Gamma_{\text{N}} - \cos 2\zeta \, \Gamma_{\text{T}} \right] \sin 2\zeta \, \Delta e^{\text{TTI}}$$
 (28)

$$\Delta C_{44}^{\text{sat}} \approx \Delta \mu_{\text{b}} - \Gamma_{\text{T}} \mu_{\text{b}} \cos^2 \zeta \, \Delta e^{\text{TTI}} \tag{29}$$

$$\Delta C_{46}^{\text{sat}} \approx \frac{1}{2} \Gamma_{\text{T}} \mu_{\text{b}} \sin 2\zeta \, \Delta e^{\text{TTI}} \tag{30}$$

$$\Delta C_{55}^{sat} \approx \Delta \mu_b - \mu_b \Big[g_{\rm d} (\sin 2\zeta)^2 \Gamma_{\rm N} + (\cos 2\zeta)^2 \Gamma_{\rm T} \Big] \Delta e^{\rm TTI} \eqno(31)$$

$$\Delta C_{66}^{\text{sat}} \approx \Delta \mu_{\text{b}} - \Gamma_{\text{T}} \mu_{\text{b}} \sin^2 \zeta \, \Delta e^{\text{TTI}}$$
 (32)

Based on the Born scattering theory (Shaw and Sen, 2004, 2006) and the first-order perturbation, the PP-wave reflection coefficient is derived by linearizing the perturbations of the stiffnesses with the scattering function, which is expressed as follows:

$$R_{\rm PP}(\theta) = \frac{1}{4\rho_0 \cos^2 \theta} S(\mathbf{r}_0) \tag{33}$$

in which

(20)

$$S(\mathbf{r}_0) = \Delta \rho \cos(2\theta) + \sum_{i=1}^{6} \sum_{j=1}^{6} \Delta C_{ij}^{\text{sat}} \xi_{ij}^{\text{PP}}$$
(34)

where ρ denotes the density of saturated rock, θ represents the incidence angle, ξ^{PP} is the related polarization vectors (Shaw and Sen, 2006), as detailed in Appendix A. Substituting Eqs. (20)–(31) into Eqs. (33) and (34) yields the linear PP-wave reflection coefficient incorporating the fluid bulk modulus, the shear modulus, the effective stress parameter, and the fracture density. It is expressed as follows:

$$R_{\rm PP}(\theta;\zeta,\Phi) = R_{\rm iso}(\theta) + R_{\rm ani}(\theta;\zeta,\Phi) \tag{35}$$

in which

$$R_{\rm iso}(\theta) = k_{K_{\rm f}}(\theta) \frac{\Delta K_{\rm f}}{\overline{K_{\rm f}}} + k_{\mu_{\rm b}}(\theta) \frac{\Delta \mu_{\rm b}}{\overline{\mu_{\rm b}}} + k_{\sigma_{\rm E}}(\theta) \frac{\Delta \sigma_{\rm E}}{\overline{\sigma_{\rm E}}} + k_{F_{\rm d}}(\theta) \frac{\Delta F_{\rm d}}{\overline{F_{\rm d}}}$$
(36)

$$R_{\rm ani}^{\rm TTI}(\theta;\zeta,\Phi) = k_{e^{\rm TTI}}(\theta;\zeta,\Phi)\Delta e^{\rm TTI} \tag{37}$$

$$k_{K_{\rm f}}(\theta) = \left(\frac{\tan^2 \theta}{2} - \frac{g_{\rm s}}{4g_{\rm d}} \sec^2 \theta\right)$$
 (38)

$$k_{\mu_{\rm b}}(\theta) = \left(\frac{g_{\rm s}}{4g_{\rm d}}\sec^2\theta - 2g_{\rm s}\sin^2\theta\right) \tag{39}$$

$$k_{\sigma_{\rm E}}(\theta) = \left(\frac{\sec^2 \theta}{4} - \frac{g_{\rm S}}{4g_{\rm d}} \sec^2 \theta\right) \tag{40}$$

$$k_{F_{\rm d}}(\theta) = \left(\frac{1}{2} - \frac{\sec^2 \theta}{4}\right) \tag{41}$$

$$k_{e^{\text{TT}}}(\theta; \Phi, \zeta) = \frac{4g_{s}}{3} \left\{ \frac{1}{g_{d}(1 - g_{d})} \left[-\frac{1}{4g_{d}} \sec^{2}\theta \left(1 - 2g_{d} \sin^{2}\theta\right)^{2} + 2g_{d} \left(\cos^{2}\theta + \sin^{2}\theta \cos^{2}\Phi\right) \sin^{2}\zeta + (1 - 2g_{d}) \left(1 - \tan^{2}\theta \cos^{2}\Phi\right) \sin^{2}\zeta - g_{d} \cos^{2}\theta \left(1 + \tan^{2}\theta \cos^{2}\Phi\right)^{2} \sin^{4}\zeta \right] + \frac{4}{(3 - 2g_{d})} \left[\sin^{2}\theta - \left(1 + \tan^{2}\theta \cos^{2}\Phi\right) \sin^{2}\zeta + \cos^{2}\theta \left(1 + \tan^{2}\theta \cos^{2}\Phi\right)^{2} \sin^{4}\zeta \right] \right\}$$

$$(42)$$

where $R_{\rm PP}$ denotes the PP-wave reflection coefficient, $F_{\rm d}=\rho K_{\rm f}$, the parameters Φ and ζ represent the azimuth and the fracture inclination angle, respectively, as illustrated in Fig. 1, and $g_{\rm S}$ represents the P- to S-wave velocity ratio in saturated anisotropic rock.

When the fracture inclination angle is 90° , etc., $\zeta = 90^{\circ}$, the anisotropic TTI medium reduces to an HTI medium with a horizontal axis of fracture symmetry. Consequently, Eq. (37) can be simplified to derive the direct seismic inversion reflection coefficient equation for vertical fracture density, which is expressed as

$$R_{\text{ani}}^{\text{HTI}}(\theta; \Phi) = k_{\rho^{\text{HTI}}}(\theta; \Phi) \Delta e^{\text{HTI}}$$
(43)

coefficients proposed by Ma et al. (2023), denoted as MA. It can be concluded that the proposed equation in Eq. (35) preserves the sufficiently high precision for seismic inversion.

The accuracy analysis of the PP-wave reflection coefficient versus incidence angle for different azimuths is shown in Figs. 2(a), 3(a) and 4(a), respectively, including azimuths of 0° (blue), 45° (green) and 90° (red). Similarly, Figs. 2(b), 3(b) and 4(b) show the accuracy analysis of reflection coefficients as a function of azimuth for different incidence angles, with incidence angles of 15° (blue), 25° (green), and 35° (red). The results demonstrate that the newly derived equation achieves high accuracy for incidence angles less than 40° . Moreover, the anisotropy induced by fractures becomes

$$k_{e^{\rm HII}}(\theta; \Phi) = \frac{4g_{\rm s}}{3} \left\{ -\frac{\sec^2 \theta}{4g_{\rm d}^2(1 - g_{\rm d})} \left[1 - 2g_{\rm d} \left(\sin^2 \theta \sin^2 \Phi + \cos^2 \theta \right) \right]^2 + \frac{4}{(3 - 2g_{\rm d})} \sin^2 \theta \cos^2 \Phi \left(1 - \tan^2 \theta \sin^2 \Phi \right) \right\}$$
(44)

where e^{HTI} denotes the fracture density in the HTI medium.

When the fracture inclination angle is 0° , etc., $\zeta=0^{\circ}$, the anisotropic TTI medium reduces to a VTI medium with a vertical axis of fracture symmetry. In this case, Eq. (36) can be simplified to derive the direct seismic inversion reflection coefficient for horizontal fracture density, which is expressed as

$$R_{\text{ani}}^{\text{VTI}}(\theta) = k_{e^{\text{VTI}}}(\theta) \Delta e^{\text{VTI}}$$
 (45)

$$k_{e^{\text{VII}}}(\theta) = \frac{4g_{\text{s}}}{3} \left\{ -\frac{\sec^2 \theta}{4g_{\text{d}}^2 (1 - g_{\text{d}})} \left(1 - 2g_{\text{d}} \sin^2 \theta \right)^2 + \frac{4 \sin^2 \theta}{(3 - 2g_{\text{d}})} \right\}$$
(46)

where e^{VTI} denotes the fracture density in the VTI medium.

To verify the accuracy of the new equation in Eq. (35), an anisotropic two-layer model is constructed to calculate the PP-wave reflection coefficient and compare it with the results obtained from the two-phase solid-liquid decoupling equation by Ma et al. (2023). The upper layer of the model is an unfractured isotropic medium, and the lower layer is an anisotropic TTI medium with a fracture density $e^{\rm TTI}$ of 0.08. Other key parameters, including P-wave velocity $\alpha^{\rm sat}$, shear modulus $\mu_{\rm b}$, S-wave velocity $\beta^{\rm sat}$, saturated rock density ρ , bulk modulus of dry rock $K_{\rm d}$, fluid bulk modulus $K_{\rm f}$, and effective stress parameter $\sigma_{\rm E}$ are listed in Table 1. Figs. 2–4 exhibit the reflection coefficient for fracture inclination angles of 30°, 60°, and 90°, respectively. In each figure, the dashed lines represent the results derived from the equation proposed in this study, while the solid lines correspond to the exact reflection

nearly negligible when the fracture inclination angle is smaller than 30° , as shown in Fig. 2.

The variation of the PP-wave reflection coefficient in Eq. (35) with respect to azimuths and incidence angles can be characterized by different reflection coefficient components. These include the fluid bulk modulus reflection coefficient, shear modulus reflection coefficient, effective stress parameter reflection coefficient, and the Fd reflection coefficient, which are shown in Fig. 5(a)–(d), respectively. The anisotropic fracture density reflection coefficients at different fracture inclination angles are shown in Fig. 5(e)-(h), respectively. These reflection coefficient terms all vary from -0.3 to 0.3 along the direction of black arrows at intervals of 0.15. The fluid bulk modulus reflection coefficient in Fig. 5(a) and the effective stress reflection coefficient in Fig. 5(c) both increase as the incidence angle increases, indicating that large incidence angles are more beneficial for inverting the effective stress parameter. Smaller incidence angles are more advantageous for the S-wave modulus in Fig. 5(b) and the parameter F_d in Fig. 5(d), which are not the primary focus of the inversion. The fracture density in Fig. 5(e)-(h) exhibits azimuthal anisotropy, and this anisotropy becomes more pronounced as the incidence angle and fracture inclination angle increase, suggesting that larger incidence angles are more effective in decoupling the fracture density at higher fracture inclination angles.

2.2. Inversion method based on L_p quasi-norm sparsity constraint

To effectively invert the fluid bulk modulus, effective stress parameter, and fracture density from the OVT domain seismic data using Eqs. (36) and (37), the azimuthal amplitude difference seismic data are utilized to invert anisotropic fracture density, as

Table 1The key elasticity and fracture parameters of the two-layer model.

	Layer	$\alpha^{\rm sat}$, km/s	$\beta^{\rm sat}$, km/s	ρ , g/cc	$\mu_{ m b}$, GPa	K _d , GPa	$K_{\rm f}$, GPa	$\sigma_{\rm E}$, v/v	e ^{TTI} , v/v
Model	Isotropic	4.82	3.14	2.52	9.98	25.0	0.10	0.11	0
	TTI	4.15	2.47	2.45	3.0	15.0	2.38	0.23	0.08

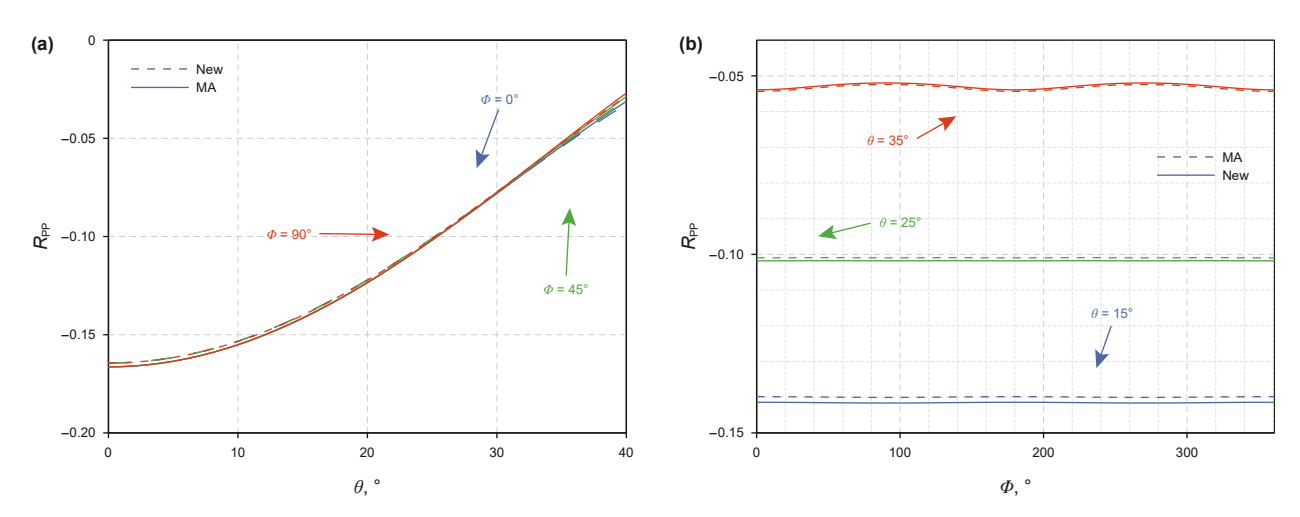


Fig. 2. Accuracy analysis of the PP-wave reflection coefficient for the fracture inclination angle ζ of 30°, where the reflection coefficient varies with (a) incidence angles for different azimuths and (b) azimuths for different incidence angles.

described in Eq. (37). Additionally, the residual seismic amplitude data are employed to invert the isotropic parameters, including fluid bulk modulus, shear modulus, and effective stress parameter, as described in Eq. (36). The two-step inversion strategy can effectively reduce the number of parameters and enhance the inversion accuracy of weakly anisotropic parameters, particularly fracture density (Zhao et al., 2024; Qin et al., 2022; Pan et al., 2020b; Chen et al., 2017). Neglecting minor azimuthal differences in wavelets, the objective function for seismic inversion based on L_p quasi-norm sparsity constraint in the time domain, is expressed as follows:

$$J(\boldsymbol{L}_{\mathrm{ani}}) = \min_{\boldsymbol{L}_{\mathrm{ani}}} \left\{ \left\| \Delta \boldsymbol{S}_{\mathrm{T}} - \boldsymbol{G}_{\mathrm{T}} \boldsymbol{D}_{0} \boldsymbol{L}_{\mathrm{ani}} \right\|_{2}^{2} \right\}$$
 in which

$$\Delta \mathbf{S_T} = \begin{bmatrix} \mathbf{s}(\theta_1, \Phi_2) - \mathbf{s}(\theta_1, \Phi_1) \\ \mathbf{s}(\theta_2, \Phi_2) - \mathbf{s}(\theta_2, \Phi_1) \\ \vdots \\ \mathbf{s}(\theta_m, \Phi_2) - \mathbf{s}(\theta_m, \Phi_1) \end{bmatrix}_{mn \times 1}$$

$$(48)$$

$$G_{\mathbf{T}} = W_0 P(\theta_i)$$

$$\mathbf{W}_{0}(\theta_{i}) = \begin{bmatrix} w_{1}^{\theta_{i}} & 0 & \cdots & 0 \\ \vdots & w_{1}^{\theta_{i}} & \ddots & \vdots \\ w_{\text{th}}^{\theta_{i}} & \vdots & \ddots & 0 \\ 0 & w_{\text{th}}^{\theta_{i}} & \cdots & w_{1}^{\theta_{i}} \\ \vdots & \vdots & \ddots & \vdots \\ 0 & \cdots & 0 & w_{\text{th}}^{\theta_{i}} \end{bmatrix}_{(t-1)\times(t-1)}$$
(50)

$$\mathbf{P}(\theta_{i};\zeta) = \begin{bmatrix} k_{e^{\Pi\Pi}}^{\mathrm{ani}}(\theta_{i};\zeta) & & & \\ & k_{e^{\Pi\Pi}}^{\mathrm{ani}}(\theta_{i};\zeta) & & & \\ & & \ddots & & \\ & & & k_{e^{\Pi\Pi}}^{\mathrm{ani}}(\theta_{i};\zeta) \end{bmatrix}_{(t-1)\times(t-1)}$$

$$(51)$$

$$k_{e^{\text{TTI}}}^{\text{ani}}(\theta_i; \zeta) = k_{e^{\text{TTI}}}(\theta_i, \Phi_2; \zeta) - k_{e^{\text{TTI}}}(\theta_i, \Phi_1; \zeta)$$
(52)

$$\mathbf{D}_{0} = \begin{bmatrix} -1 & 1 & 0 & \cdots & 0 \\ 0 & -1 & 1 & \ddots & \vdots \\ \vdots & \ddots & \ddots & \ddots & 0 \\ 0 & \cdots & \cdots & -1 & 1 \end{bmatrix}_{(t-1)\times t}$$
(53)

$$\boldsymbol{L}_{\text{ani}} = \begin{bmatrix} \left(e^{\text{TTI}} \right)_1 & \left(e^{\text{TTI}} \right)_2 & \dots & \left(e^{\text{TTI}} \right)_t \end{bmatrix}_{t \times 1}^{\text{T}}$$
(54)

where $\Delta \mathbf{S}_{\mathrm{T}}$ denotes the azimuthal amplitude difference seismic data between azimuth Φ_1 and azimuth Φ_2 , the matrix transpose

(49)

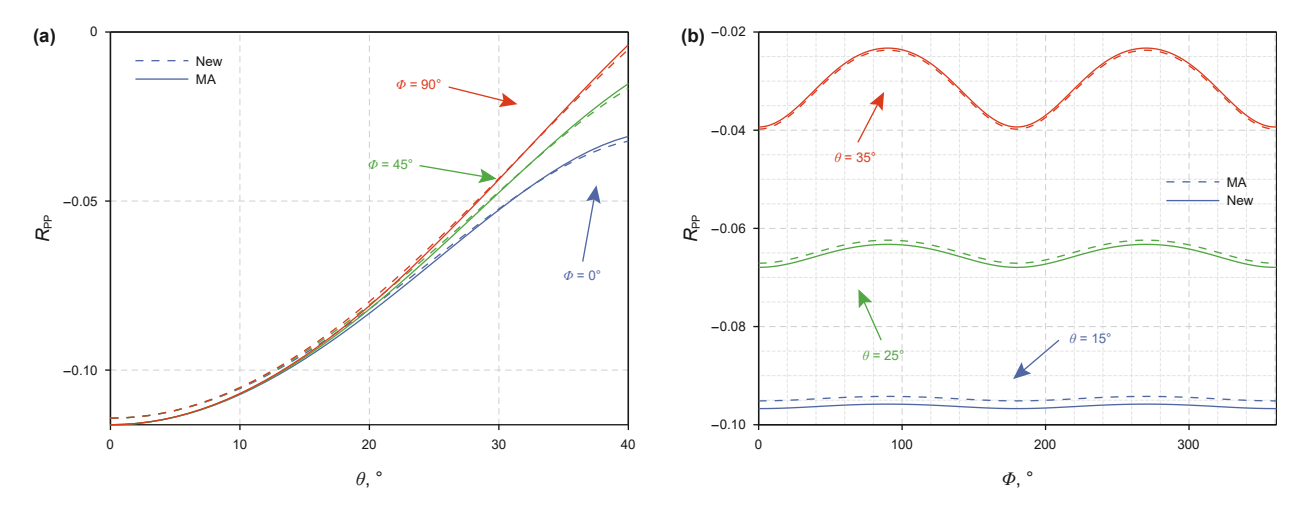


Fig. 3. Accuracy analysis of the PP-wave reflection coefficient for the fracture inclination angle ζ of 60° , where the reflection coefficient varies with (a) incidence angles for different azimuths and (b) azimuths for different incidence angles.

operator G_T denotes the forward operator, $\|\cdot\|_2$ represents L2-norm, $L_{\rm ani}$ is the inversion parameter matrix composed of the anisotropic fracture density, W_0 , D_0 , and P represent the wavelet matrix, the first-order difference matrix, and the angle coefficient matrix, respectively, the subscripts "t" and "m" represent the number of vertical sampling points and incidence angles, respectively, and the superscript "T" represents the transpose of the matrix.

The low-frequency model constraint term is designed to provide more background information for the parameters, enabling the inversion to be more stable. Additionally, the L_p quasi-norm sparsity constraint term is utilized to characterize the sparsity of the PP-wave reflection coefficient, improving the inversion vertical resolution. Therefore, the objective function for seismic inversion based on L_P quasi-norm sparsity constraint in this article is given as

$$J(\boldsymbol{L}_{\text{ani}}) = \min_{\boldsymbol{L}_{\text{ani}}} \left\{ \|\Delta \boldsymbol{S}_{\text{T}} - \boldsymbol{G}_{\text{T}} \boldsymbol{D}_{0} \boldsymbol{L}_{\text{ani}} \|_{2}^{2} + \kappa_{1} \|\boldsymbol{L}_{\text{ani}} - \boldsymbol{L}_{\text{ani}}^{\text{low}} \|_{2}^{2} + \eta_{1} \|\boldsymbol{P} \boldsymbol{D}_{0} \boldsymbol{L}_{\text{ani}} \|_{p}^{p} \right\}$$

$$(55)$$

where $\|\|_p$ represents L_p quasi-norm, in which $p \in (0, 1)$, κ_1 and η_1 represent the weights of the low-frequency and sparse constraint

terms, respectively, and $\boldsymbol{L}_{ani}^{low}$ denotes the initial model matrix with low frequency. Then, the Lagrange multiplier \boldsymbol{L}_{m} and dual term \boldsymbol{C}_{d} are inserted to transform the nonlinear problem in Eq. (56) into the constrained linear optimization problem, as follows:

$$J(\boldsymbol{L}_{\text{ani}}) = \min_{\boldsymbol{L}_{\text{ani}}} \left\{ \|\Delta \boldsymbol{S}_{\text{T}} - \boldsymbol{G}_{\text{T}} \boldsymbol{D}_{0} \boldsymbol{L}_{\text{ani}} \|_{2}^{2} + \kappa_{1} \|\boldsymbol{L}_{\text{ani}} - \boldsymbol{L}_{\text{ani}}^{\text{low}} \|_{2}^{2} + \eta_{1} \|\boldsymbol{L}_{\text{m}} \|_{p}^{p} + \kappa_{2} \|\boldsymbol{L}_{\text{m}} - \boldsymbol{P} \boldsymbol{D}_{0} \boldsymbol{L}_{\text{ani}} + \boldsymbol{C}_{\text{d}} \|_{2}^{2} \right\}$$

$$(56)$$

where multiple single-parameter optimization problems can be given by the alternating direction multiplier method (ADMM):

$$J(\mathbf{L}_{ani}) = \min_{\mathbf{L}_{ani}} \left\{ \|\Delta \mathbf{S}_{T} - \mathbf{G}_{T} \mathbf{D}_{0} \mathbf{L}_{ani}\|_{2}^{2} + \kappa_{1} \|\mathbf{L}_{ani} - \mathbf{L}_{ani}^{low}\|_{2}^{2} + \kappa_{2} \|\mathbf{L}_{m} - \mathbf{P} \mathbf{D}_{0} \mathbf{L}_{ani} + \mathbf{C}_{d}\|_{2}^{2} \right\}$$
(57)

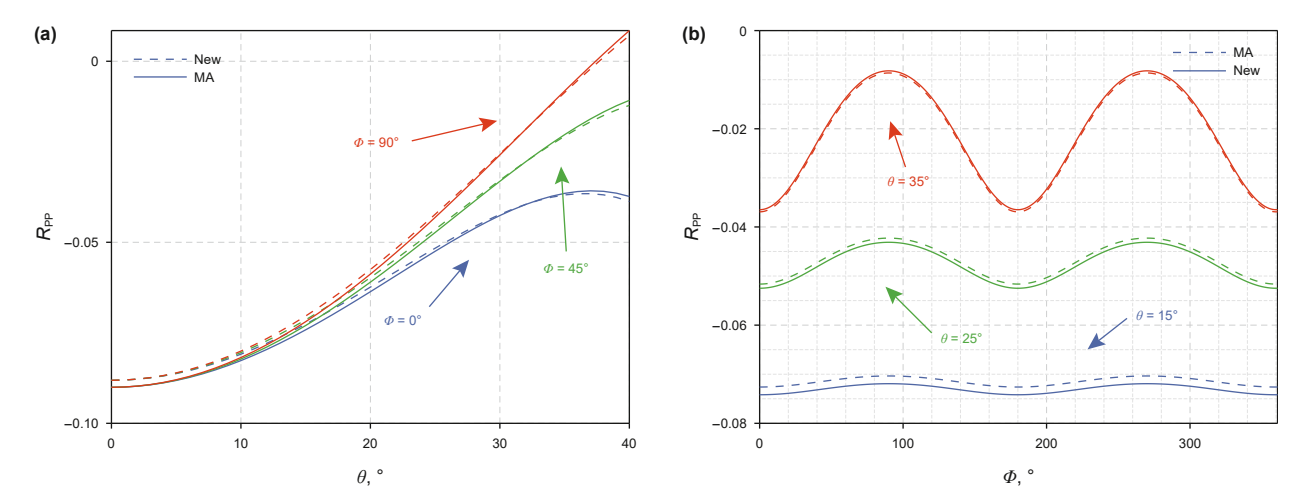


Fig. 4. Accuracy analysis of the PP-wave reflection coefficient for the fracture inclination angle ζ of 90°, where the reflection coefficient varies with (a) incidence angles for different azimuths and (b) azimuths for different incidence angles.

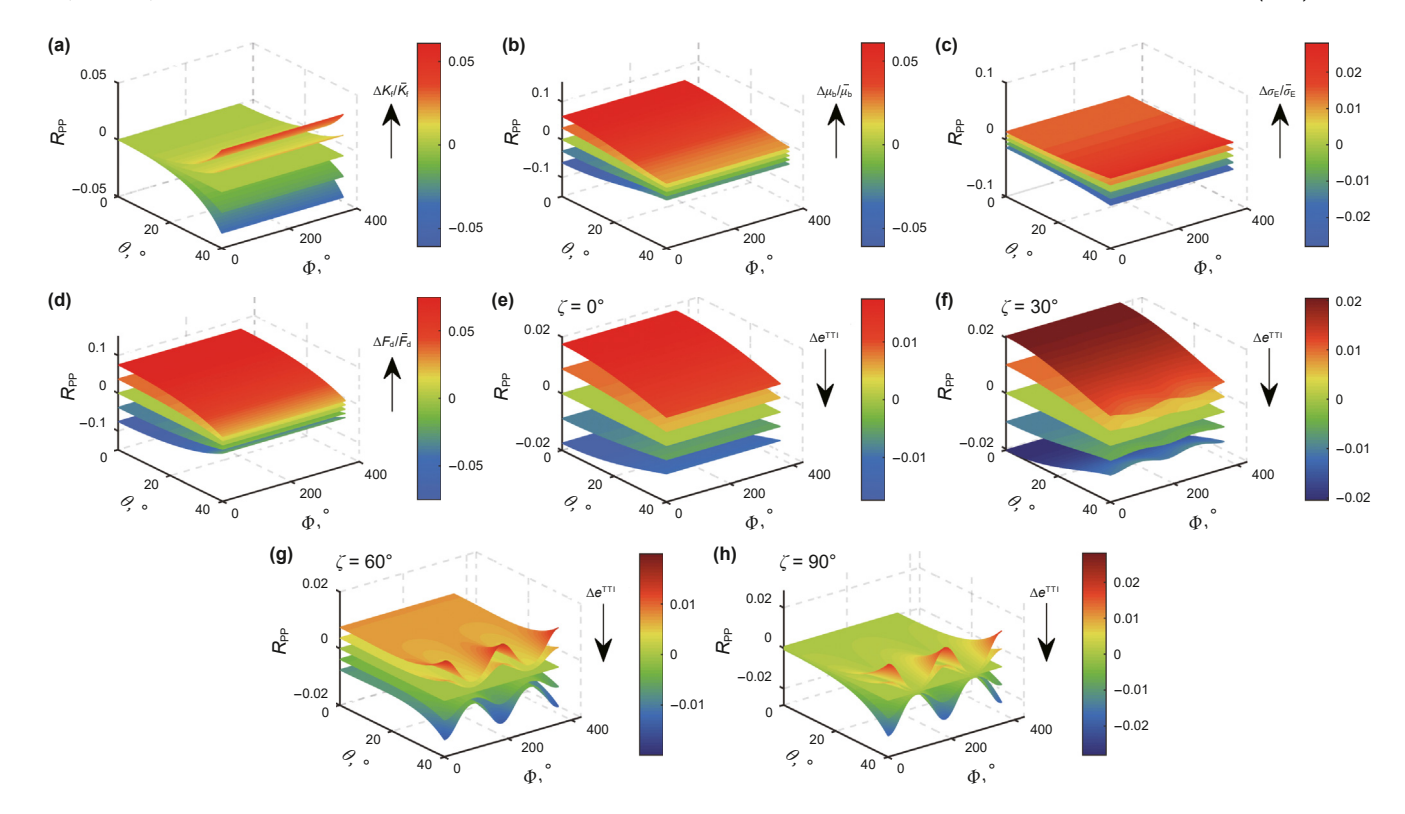


Fig. 5. Sensitivity and contribution characterization of different reflection coefficient terms, where (a) fluid bulk modulus reflection coefficient, (b) shear modulus reflection coefficient, (c) effective stress parameter reflection coefficient, (d) F_d reflection coefficient, (e) – (f) tilted fracture density reflection coefficient for fracture inclination angles of 0° , 30° , 60° , and 90° , respectively.

$$J(\mathbf{L}_{m}) = \min_{\mathbf{L}_{m}} \left\{ \eta_{1} \|\mathbf{L}_{m}\|_{p}^{p} + \kappa_{2} \|\mathbf{L}_{m} - \mathbf{P} \mathbf{D}_{0} \mathbf{L}_{ani} + \mathbf{C}_{d}\|_{2}^{2} \right\}$$
 (58)

$$J(\boldsymbol{C}_{d}) = \min_{\boldsymbol{C}} \left\{ \kappa_{2} \|\boldsymbol{L}_{m} - \boldsymbol{P}\boldsymbol{D}_{0}\boldsymbol{L}_{ani} + \boldsymbol{C}_{d}\|_{2}^{2} \right\}$$
 (59)

We then solve each unconstrained subproblem separately to obtain their iteratively updated expressions:

$$\mathbf{L}_{\text{ani}}^{(k+1)} = \left\{ (\mathbf{W}_0 \mathbf{P} \mathbf{D})^{\text{T}} \mathbf{W}_0 \mathbf{P} \mathbf{D} + \kappa_1 \mathbf{I} + \kappa_2 \left[(\mathbf{P} \mathbf{D})^{\text{T}} \mathbf{P} \mathbf{D} \right] \right\}^{-1} \cdot \left\{ (\mathbf{W}_0 \mathbf{P} \mathbf{D})^{\text{T}} \Delta \mathbf{S}_{\text{T}} + \kappa_1 \mathbf{L}_{\text{ani}}^{\text{low}} + \kappa_2 (\mathbf{P} \mathbf{D})^{\text{T}} \left[\mathbf{L}_{\text{m}}^{(k)} - \mathbf{C}_{\text{d}}^{(k)} \right] \right\}$$
(60)

$$\begin{split} & \boldsymbol{L_{m}}^{(k+1)} \!=\! sign\!\left[\!\boldsymbol{PDL}_{ani}^{(k+1)} \!+\! \boldsymbol{C_{d}}^{(k)}\right] \\ & \cdot max\!\left[\!\left|\!\boldsymbol{PDL}_{ani}^{(k+1)} \!+\! \boldsymbol{C_{d}}^{(k)}\right| \!-\! \left(\!\frac{\kappa_{2}}{\eta_{1}}\!\right)^{p-2} \!\left|\!\boldsymbol{PDL}_{ani}^{(k+1)} \!+\! \boldsymbol{C_{d}}^{(k)}\right|^{p-1}, 0\right] \end{split}$$

$$\mathbf{C_d}^{(k+1)} = \mathbf{C_d}^{(k)} + \left[\mathbf{PDL}_{ani}^{(k+1)} - \mathbf{L}_{m}^{(k+1)} \right]$$
 (62)

The above Eqs. (60)–(62) can be iteratively solved for the parameter matrix about the fracture density. The second step inversion can use the remaining seismic data, eliminating the anisotropic component to invert the isotropic parameters by traditional amplitude variation with offset (AVO) inversion method. L_{iso} can replace the inversion parameter matrix, which is detailed as

$$\mathbf{L}_{\text{iso}} = \ln \begin{bmatrix} \mathbf{K}_{\text{f}} & \boldsymbol{\mu}_{\text{b}} & \boldsymbol{\sigma}_{\text{E}} & \mathbf{F}_{\text{d}} \end{bmatrix}_{(4t) \times 1}^{\text{T}}$$
(63)

in which

$$\mathbf{K}_{\mathbf{f}} = \left[\begin{pmatrix} K_{\mathbf{f}} \end{pmatrix}_{1} & \begin{pmatrix} K_{\mathbf{f}} \end{pmatrix}_{2} & \dots & \begin{pmatrix} K_{\mathbf{f}} \end{pmatrix}_{t} \right]_{t \times 1}$$
(64)

$$\mu_{b} = [(\mu_{b})_{1} \quad (\mu_{b})_{2} \quad \dots \quad (\mu_{b})_{t}]_{t \times 1}$$
(65)

$$\boldsymbol{\sigma}_{E} = [(\sigma_{E})_{1} \quad (\sigma_{E})_{2} \quad \dots \quad (\sigma_{E})_{t}]_{t \times 1}$$
(66)

$$\mathbf{F}_{d} = [(F_{d})_{1} \quad (F_{d})_{2} \quad \dots \quad (F_{d})_{t}]_{t \times 1}$$
 (67)

where the symbol "In" denotes the natural logarithm operation. It is then solved using the same inversion algorithm as described above. The workflow of the seismic inversion algorithm based on the L_p quasi-norm sparsity constraint is summarized in Table 2.

3. Model testing and filed application

3.1. Model testing

The modeling tests are designed to evaluate the capability of the inversion method described in Section 2.2 to directly decouple the fluid bulk modulus, effective stress parameter, and fracture density. Seismic data with different azimuths and incidence angles are first synthesized using convolutional modeling with a 30 Hz Ricker wavelet. Seismic datasets with varying SNRs are then generated by adding various levels of Gaussian random noise, including noise-free data in Fig. 7, an SNR of 5 in Fig. 8, and an SNR of 2 in Fig. 6. The azimuths range from 0° to 150° at 30° intervals. The incidence

Table 2 Seismic inversion algorithm of anisotropic and isotropic parameters based on L_p quasi-norm sparsity constraint.

Pseudocode: Pre-stack seismic inversion of elasticity and fracture parameters based on ADMM and iterative shrinkage thresholding algorithm (ISTA)

```
Step 1: Input: \Delta S_{\Gamma}, L_{\rm ani}^{\rm low}, P, D_0, W_0, \kappa_1, \kappa_2, \eta_1, p, error threshold \varepsilon. Step 2: Initial parameters: k=0, L_{\rm ani}^{\rm low}=L_{\rm ani}^{\rm low}, L_{\rm m}^{\rm lo}=0, C_{\rm d}^{\rm lo}=0. Step 3: Iteratively updated L_{\rm ani}^{(k+1)} by Eq. (60). Step 4: Iteratively updated L_{\rm m}^{(k+1)} by Eq. (61). Step 5: Iteratively updated C_{\rm low}^{(k+1)} by Eq. (62). Step 6: Termination conditions: If \{\|L_{\rm ani}^{(k+1)}-L_{\rm ani}^{(k)}\|_2/\|L_{\rm ani}^{(k)}\|_2 > \varepsilon, k=k+1, perform steps 3–5. Or, the iteration of updates ceases; perform step 7. Step 7: Obtain the parameters matrix L_{\rm ani}^{(k+1)}. Step 8: Optimal inversion results: fracture density matrix e^{\rm TTI}. Step 9: Remained seismic data inversion parameters: K_{\rm f}, \mu_{\rm b}, \sigma_{\rm E}, and F_{\rm d}.
```

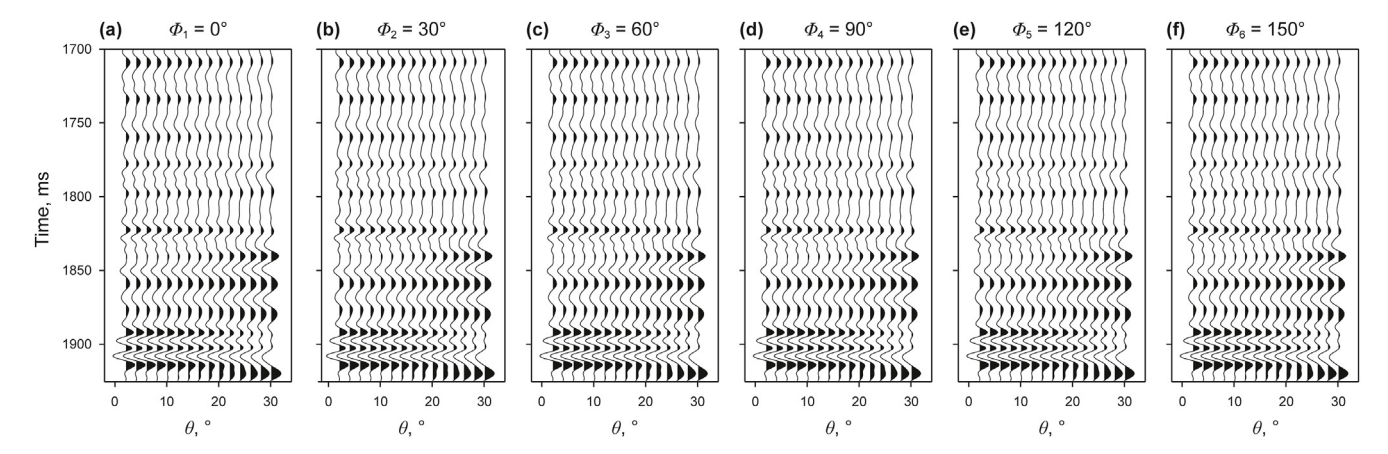


Fig. 6. Noise-free synthetic seismic data at different azimuths and incidence angles.

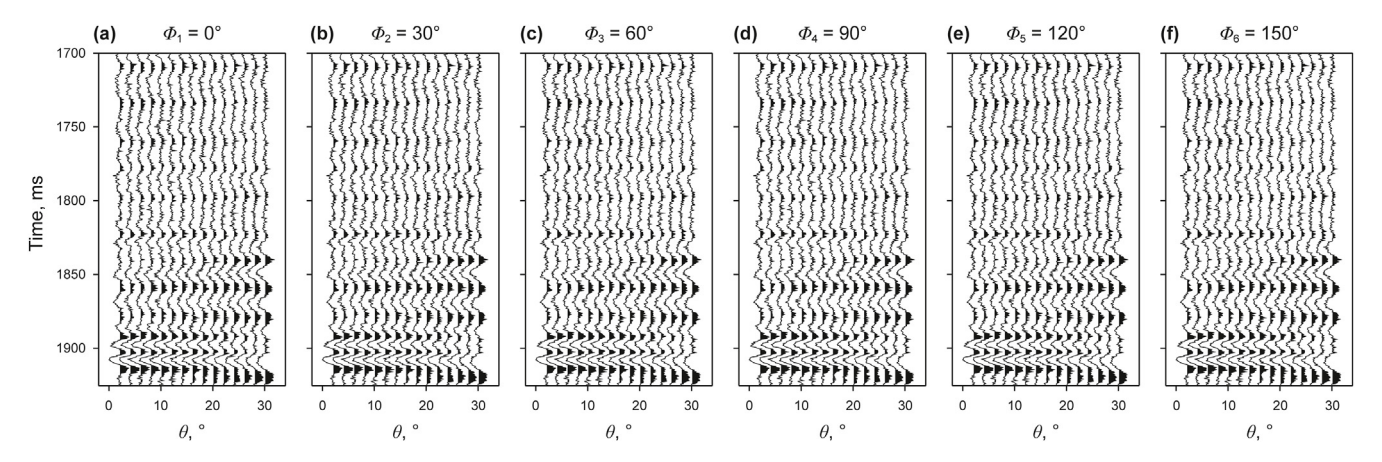


Fig. 7. Synthetic seismic data at different azimuths and incidence angles with an SNR of 5.

angles range from 2° to 30° at 2° intervals. For the noise-free seismic data in Fig. 7, the azimuthal amplitude difference seismic data in Fig. 9 can be obtained by differencing the seismic data at different azimuths. Then, the azimuthal amplitude difference seismic data with SNRs of 5 and 2 are displayed in Figs. 10 and 11, respectively. Three sets of seismic data with different SNRs are used to test the noise robustness of the inversion algorithm. Based on the azimuthal anisotropy of fracture density, azimuthal amplitude difference seismic data in Figs. 9–11 are utilized to directly invert the fracture density in the first step of the inversion.

Fig. 12 illustrates the inversion results of elasticity and fracture parameters from noise-free seismic data. The green curves represent

low-frequency models obtained by low-pass filtering the actual model curves, which serve as initial values for the inversion and supplement the background information. The blue curves represent the exact model curves. The red curves show the inversion results. The black shaded bands indicate confidence curves calculated based on actual model curves with acceptable errors within 8%. The fracture density in Fig. 12(e) exhibits a satisfactory inversion result using azimuthal amplitude difference seismic data in Fig. 9. The fluid bulk modulus in Fig. 12(a) and the effective stress parameter in Fig. 12(d) of the isotropic parameters can be inverted, with exceptionally satisfactory results. The second step inversion with more isotropic parameters involved compared to the anisotropic inversion, results

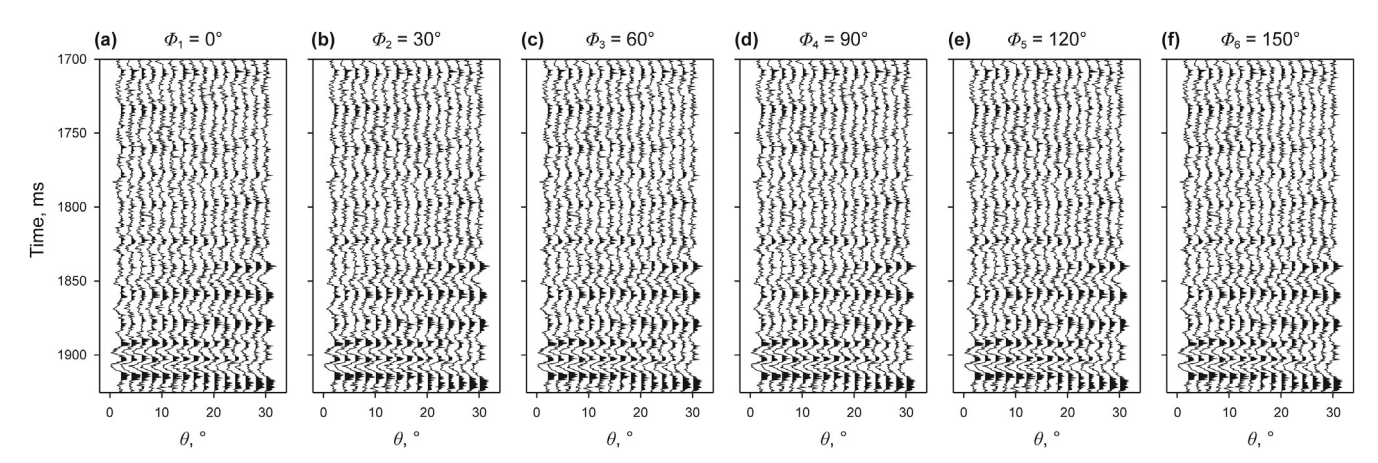


Fig. 8. Synthetic seismic data at different azimuths and incidence angles with an SNR of 2.

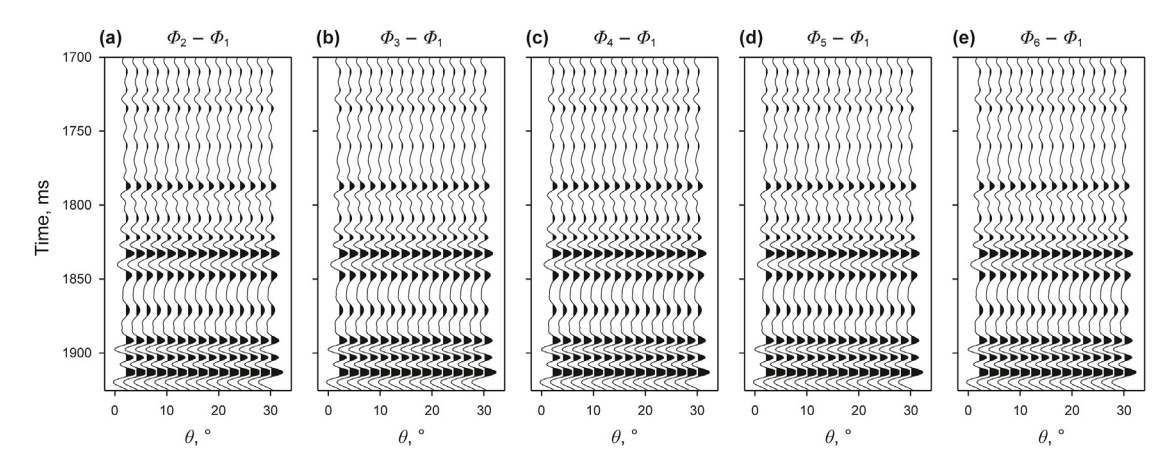


Fig. 9. Noise-free azimuthal amplitude difference seismic data.

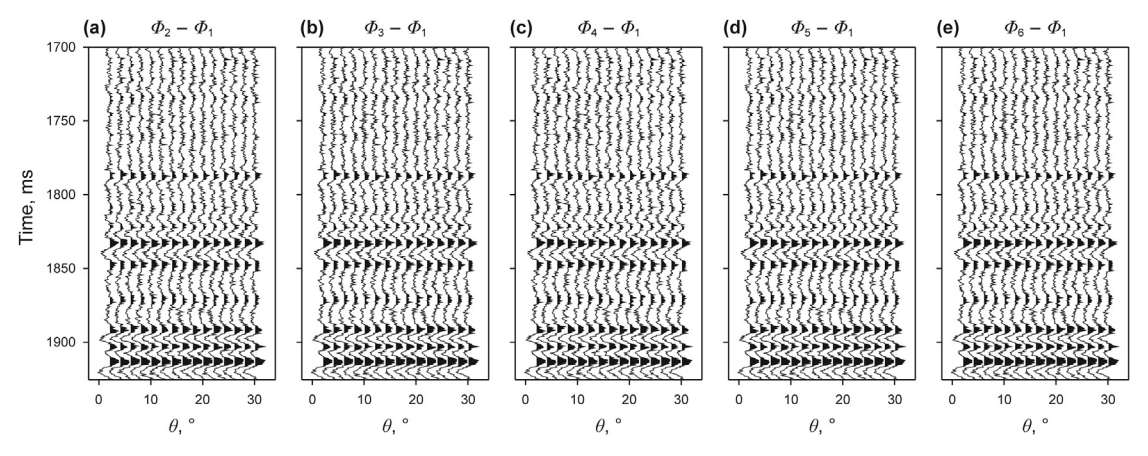


Fig. 10. Azimuthal amplitude difference seismic data with an SNR of 5.

in a certain degree of parameter interaction during the inversion process. However, the inversion results for all isotropic parameters agree remarkably well with the model curves, indicating that the inversion strategy is theoretically feasible.

Similarly, Figs. 13 and 14 illustrate the inversion results for seismic data with SNRs of 5 and 2, respectively. As the level of random noise increases, the inversion results for all parameters exhibit greater distortion (highlighted by the black arrows), and the

fracture density at shallower depths remains relatively less affected by noise. Despite the substantial decrease in the SNR of the seismic data, the inversion results for all parameters still align closely with the actual curves within an acceptable relative error. The above experiments confirm that the two-step inversion method, based on the L_P quasi-norm sparsity constraint, enables the direct seismic inversion of fluid bulk modulus, effective stress parameter, and fracture density.

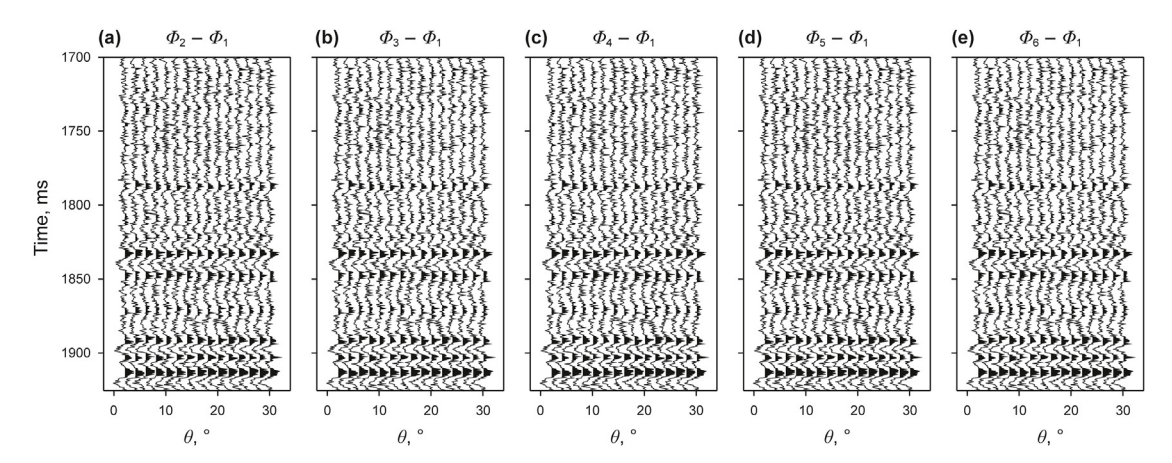


Fig. 11. Azimuthal amplitude difference seismic data with an SNR of 2.

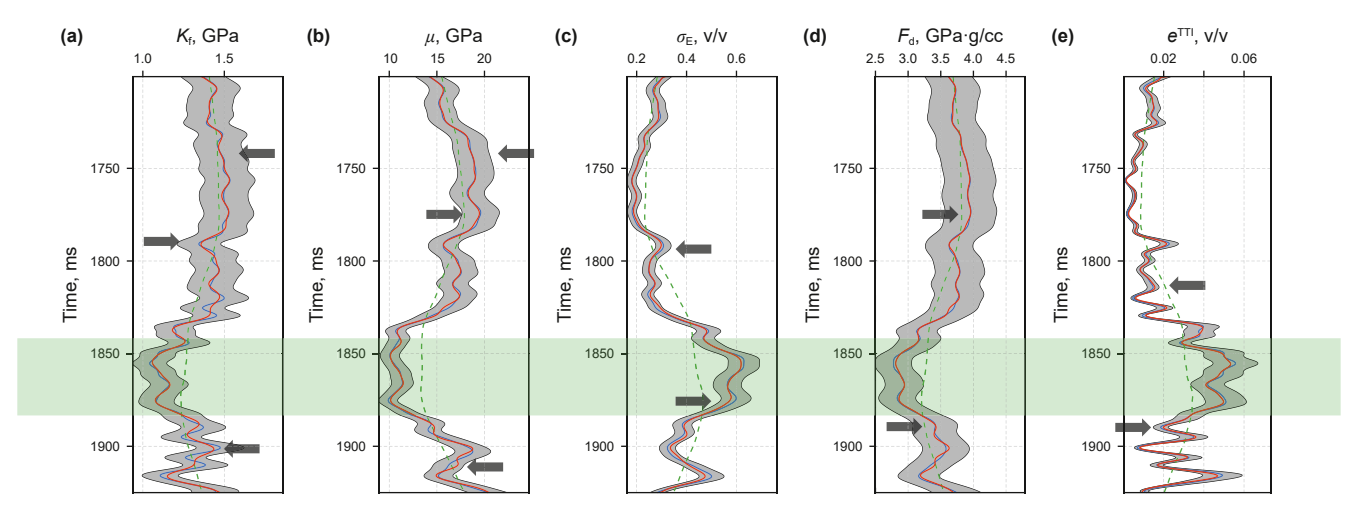


Fig. 12. Elasticity and fracture parameters inversion results for noise-free seismic data, where **(a)** fluid bulk modulus, **(b)** shear modulus, **(c)** effective stress parameter, **(d)** F_d parameter, and **(e)** tilted fracture density.

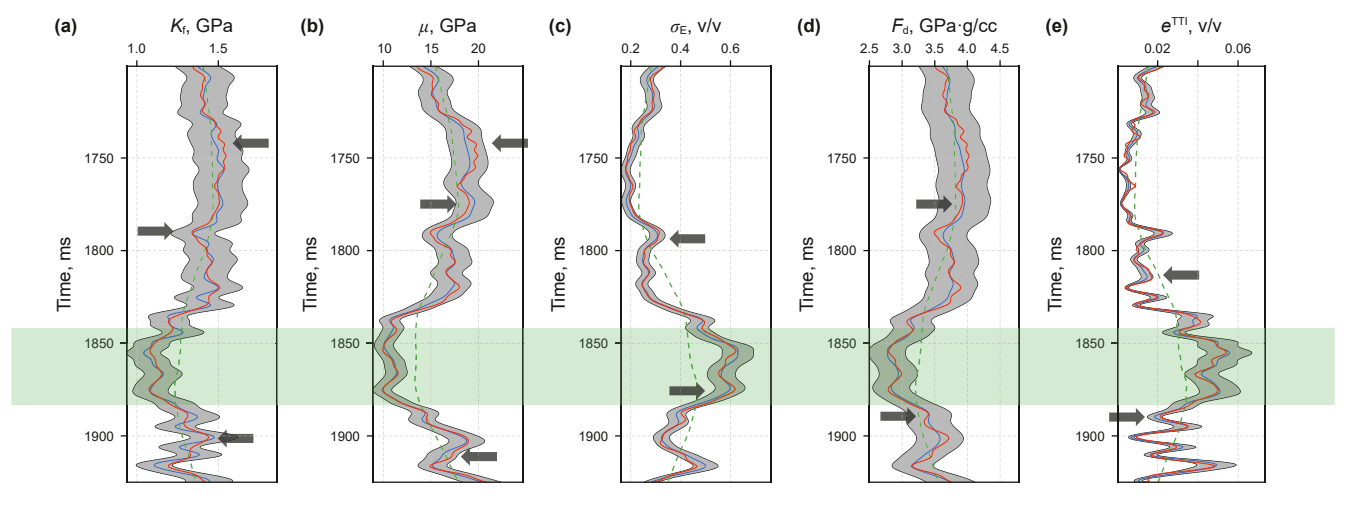


Fig. 13. Elasticity and fracture parameters inversion results for seismic data with an SNR of 5, where (a) fluid bulk modulus, (b) shear modulus, (c) effective stress parameter, (d) F_d parameter, and (e) tilted fracture density.

The evaluation metrics, including the correlation coefficient (*CC*), relative root mean square error (RRMSE), and SNR, are introduced to quantitatively assess the inversion results from the above three groups of noise-resistant model tests. The corresponding

calculations are detailed in Table 3, where $d^{\rm pre}$ represents the prediction vector, $d^{\rm obs}$ represents the observed actual model vector, t is the total sampling number, the upper line denotes the average value of the parameter, and the symbol "log₁₀" denotes the common

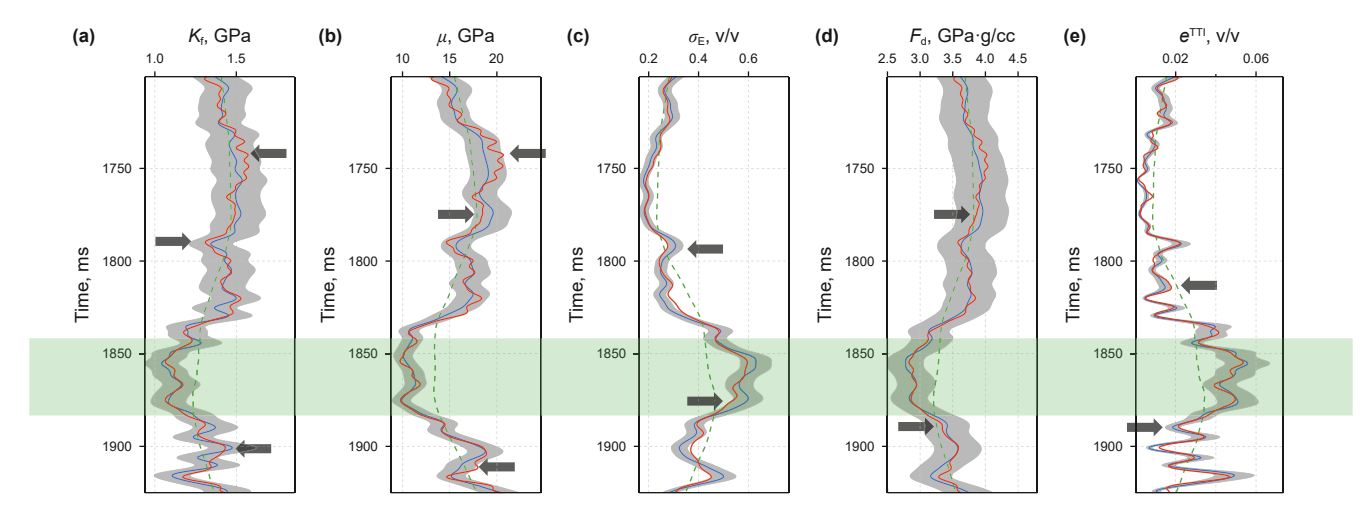


Fig. 14. Elasticity and fracture parameters inversion results for seismic data with an SNR of 2, where (a) fluid bulk modulus, (b) shear modulus, (c) effective stress parameter, (d) F_d parameter, and (e) tilted fracture density.

Table 3 Index for evaluating the effect of prediction versus observation errors.

Index	Expression	Resource
Correlation coefficient (CC)	$CC = \frac{\sum_{i=1}^{t} \left[(\boldsymbol{d}_{i}^{\text{pre}} - \overline{\boldsymbol{d}}^{\text{pre}}) (\boldsymbol{d}_{i}^{\text{obs}} - \overline{\boldsymbol{d}}^{\text{obs}}) \right]}{\sqrt{\left[\sum_{i=1}^{t} (\boldsymbol{d}_{i}^{\text{pre}} - \overline{\boldsymbol{d}}^{\text{pre}})^{2} \sum_{i=1}^{t} (\boldsymbol{d}_{i}^{\text{obs}} - \overline{\boldsymbol{d}}^{\text{obs}})^{2} \right]}} $ (68)	Zhao et al., 2024; Qin et al., 2022.
Relative root mean square error (RRMSE)	$RRMSE = \frac{1}{ \boldsymbol{d}^{obs} } \sqrt{\frac{\sum_{i=1}^{t} (\boldsymbol{d}_{i}^{pre} - \boldsymbol{d}_{i}^{obs})^{2}}{t}} $ (69)	Iftikhar et al., 2022; AL-Musaylh et al., 2021.
Signal-to-noise ratio (SNR)	$SNR = 10 \log_{10} \left[\frac{\sum_{i=1}^{t} (\boldsymbol{d}_{i}^{\text{obs}} - \overline{\boldsymbol{d}^{\text{obs}}})^{2}}{\sum_{i=1}^{t} (\boldsymbol{d}_{i}^{\text{pre}} - \overline{\boldsymbol{d}_{i}^{\text{obs}}})^{2}} \right] $ (70)	Zhao et al., 2023.

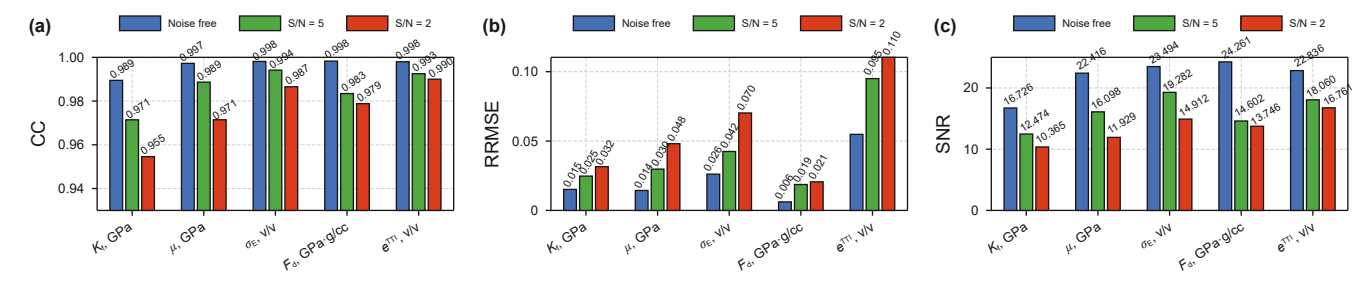


Fig. 15. Quantitative evaluation results of inversion results for different parameters in different noise conditions. (a) CC, (b) RRMSE, (c) SNR.

logarithm function. The CC quantifies the degree of correlation between the predicted and modeled values, with values approaching 1 indicating a stronger correlation. The RRMSE represents prediction error relative to the actual value, with smaller RRMSE values signifying higher inversion accuracy. The SNR represents the ratio of the predicted value to the actual value, with higher SNR values indicating better inversion performance. As the SNR the seismic data diminishes, the correlation coefficients also decrease. However, as depicted in Fig. 15(a), all CC values remain above 0.95, and the RRMSE values increase with decreasing SNR but remain below 0.1, as illustrated in Fig. 15(b). Correspondingly, the SNR of the inversion results in Fig. 15(c) decreases. The modeling tests confirm the reliability and robustness of the proposed inversion method, demonstrating its acceptable noise resistance. Further practical applications will also substantiate its effectiveness.

3.2. Field application

The study area is situated in the southwest of the Sichuan Basin, as shown in Fig. 16. The target reservoir corresponds to a fractured gas-bearing shale reservoir within the Wufeng-Longmaxi Formation. The interpretation of the fullbore formation microimager (FMI) in Fig. 17(a) demonstrates that the reservoir consists of high-angle tilted fractures, which aligns with the drilling cores in Fig. 17(b). The fractures primarily develop in a southwest-northeast direction, with a minor west-east component, as illustrated in Fig. 17(c). The fracture inclination angles predominantly cluster around 70° , as shown in Fig. 17(d). The study area features the vertical Well A, along with three horizontal wells— H_1 , H_3 , and H_5 . The essential elasticity and fracture parameters for Well A, including the associated logging and prediction curves, are shown in Fig. 18. In this figure, the

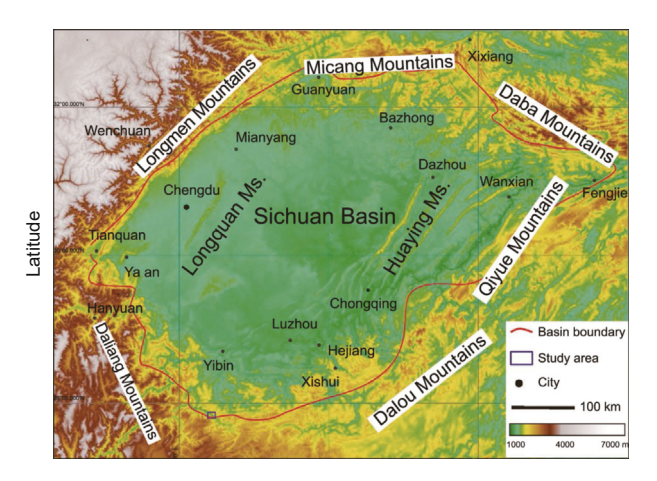


Fig. 16. Geographic location map of the study area (The study block is marked with a rectangular box, Lin et al., 2022).

markers T₁, T₂, and T₃ correspond to the different well tops, with the fractured gas-bearing shale reservoir located between well tops T₂ and T₃. This target reservoir is characterized by high fracture density in Fig. 18(g), elevated total organic carbon (TOC) in Fig. 18(h), low fluid bulk modulus in Fig. 18(d), and high effective stress parameter in Fig. 18(f). In this study, the parameter g_d is assigned as a constant value of 0.38, as determined by petrophysical modeling of fractured shale gas reservoirs (Zhao et al., 2024). To improve the SNR of seismic data and enhance the stability of the seismic inversion, we first extract the azimuthal stacked seismic data from the OVT domain seismic data based on two dominant azimuths. The seismic data are then stacked at three central incidence angles to generate central angle stacked seismic data with varying azimuths, as shown in Fig. 19. This arbitrary line contains 300 traces and covers a time range of 1.50 s-1.80 s, correlating to a time of 1.78 s at the bottom of the reservoir on Well A. After differencing the seismic data from different azimuths with the same central incidence angle, the

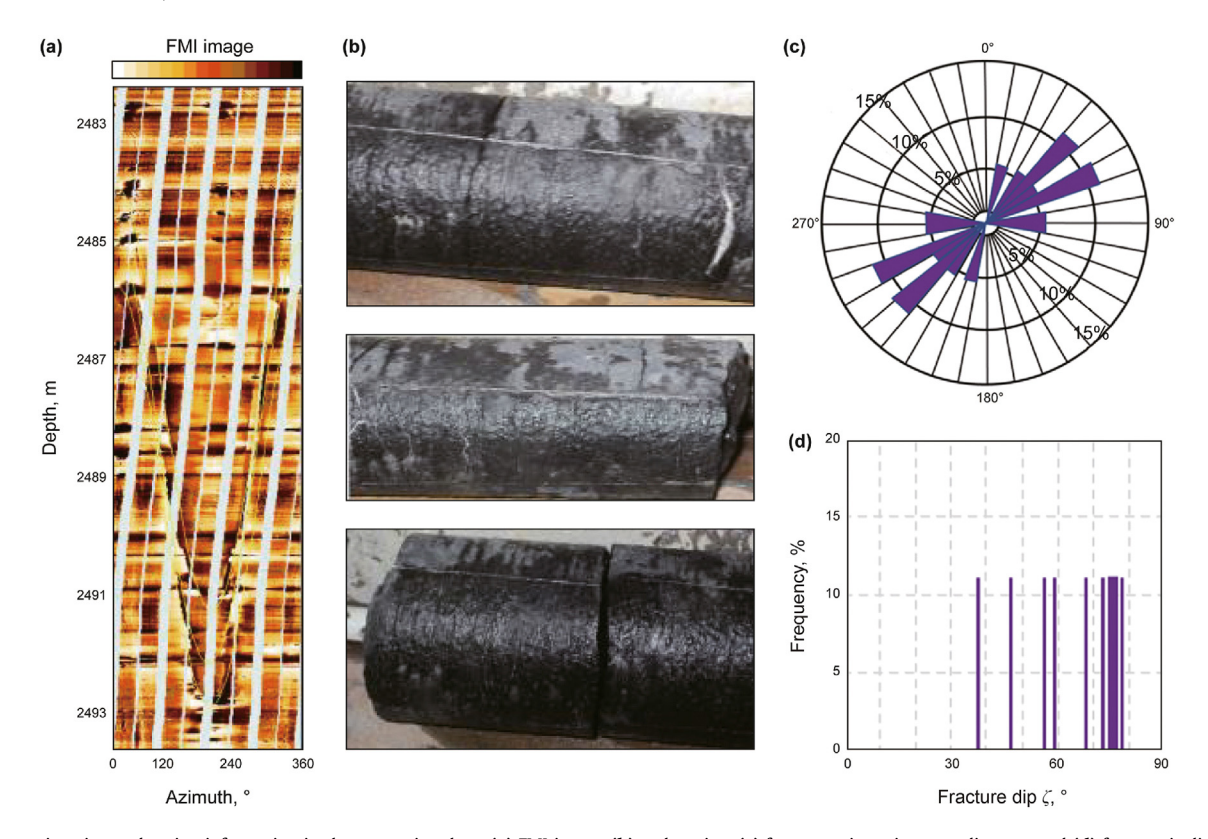


Fig. 17. Fracture imaging and coring information in the reservoir, where (a) FMI image, (b) rock coring, (c) fracture orientation rose diagram, and (d) fracture inclination angle statistics.

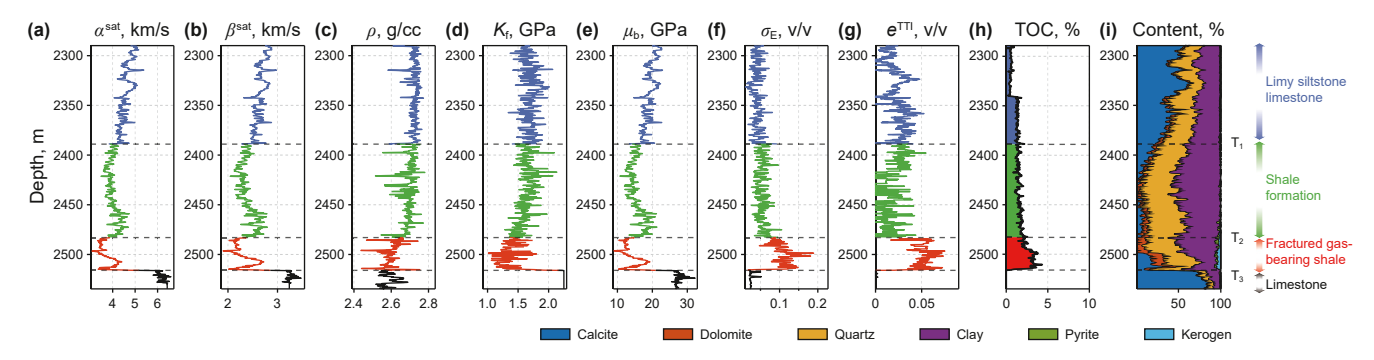


Fig. 18. Actual logging and predicted curves for Well A, where (a) P-wave velocity, (b) S-wave velocity, (c) rock density, (d) fluid bulk modulus, (e) shear modulus, (f) effective stress parameter, (g) tilted fracture density, (h) total organic carbon, and (i) mineral fraction content.

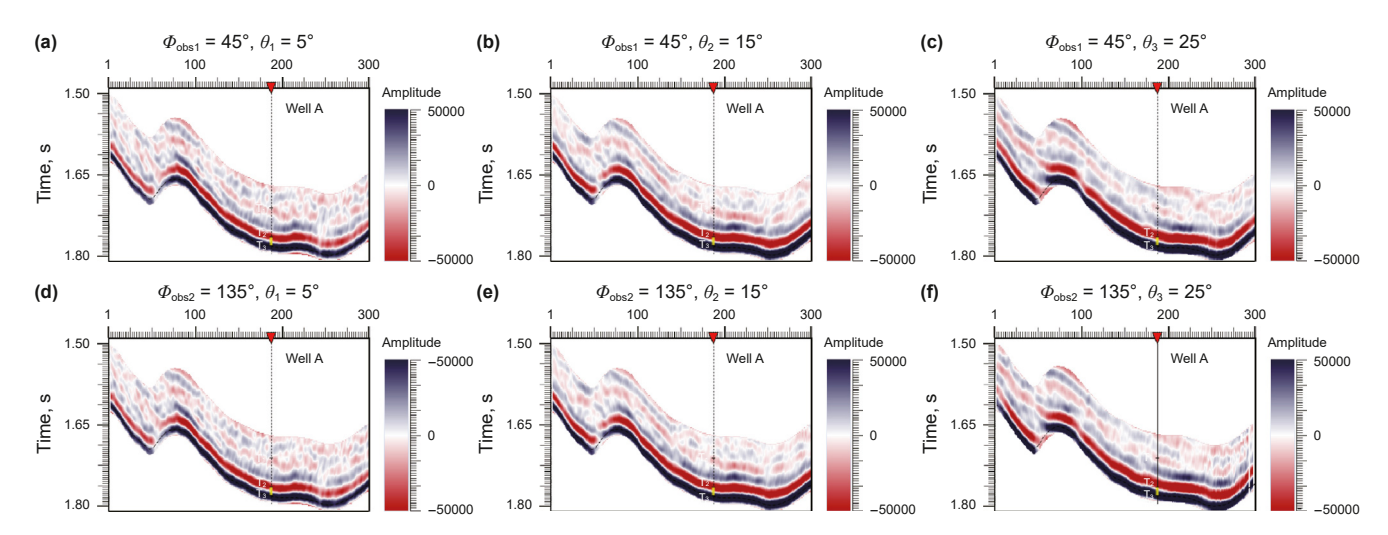


Fig. 19. Seismic stacked data from an arbitrary survey line passing through Well A, containing different azimuths and central incidence angles, where (a)–(c) $\Phi_{abs1} = 45^{\circ}$, (d)–(f) $\Phi_{abs2} = 135^{\circ}$, containing different central incidence angles (a) and (d) ccentral incidence angle $\theta_1 = 5^{\circ}$, (b) and (e) central incidence angle $\theta_2 = 15^{\circ}$, and (c) and (f) central incidence angle $\theta_3 = 25^{\circ}$.

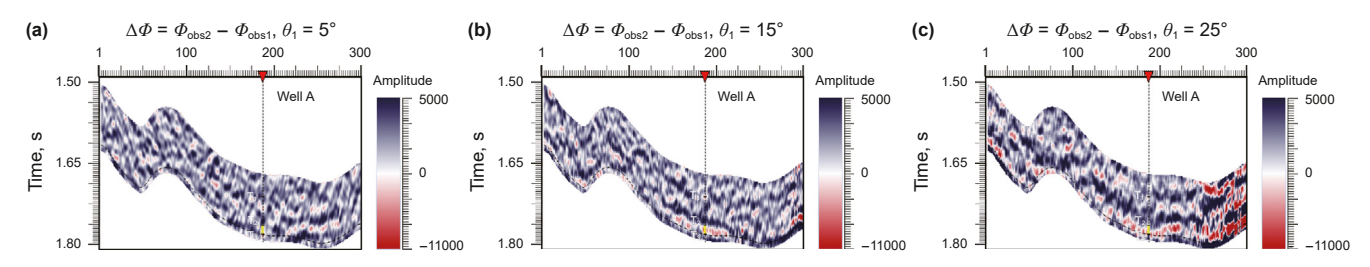


Fig. 20. Azimuthal amplitude seismic difference data for different central incident angles, where (a) central incidence angle $\theta_1 = 5^{\circ}$, (b) central incidence angle $\theta_2 = 15^{\circ}$, and (c) central incidence angle $\theta_3 = 25^{\circ}$.

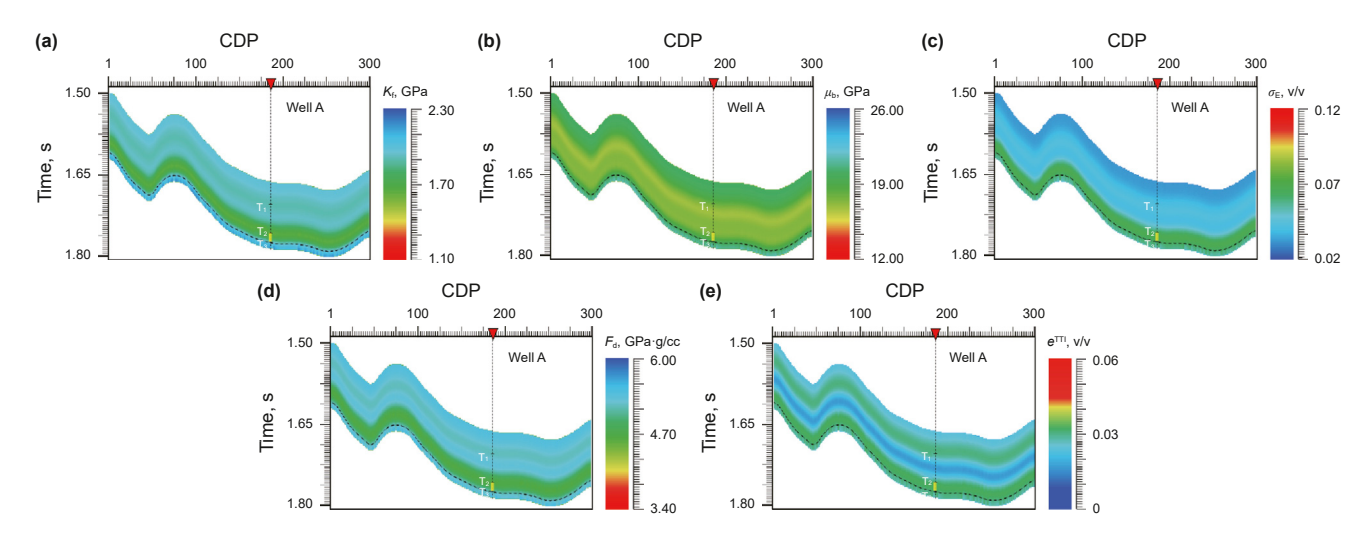


Fig. 21. Initial models of the elasticity and fracture parameters of an arbitrary survey line passing through Well A, where (a) fluid bulk modulus, (b) shear modulus, (c) effective stress parameter, (d) F_d parameter, and (e) tilted fracture density.

azimuthal amplitude difference seismic data can be further obtained, as shown in Fig. 20. Apparent amplitude anomalies are visible in the reservoir section, marked in yellow along the well path. Based on the elasticity and fracture parameters on Well A displayed in Fig. 18, interpolation, extrapolation, and Gaussian low-pass filtering can help obtain the low-frequency models of the parameters, which are used as the initial values of the seismic inversion to

improve its stability. The low-frequency models are displayed in Fig. 21.

The 2D inversion results for an arbitrary line are exhibited in Fig. 22. The fluid bulk modulus in Fig. 22(a) in the reservoir section (from well tops T_2 to T_3) inverts an apparent relatively low-value anomaly, indicating that the reservoir contains high shale gas content. The effective stress parameter in Fig. 22(c) shows high

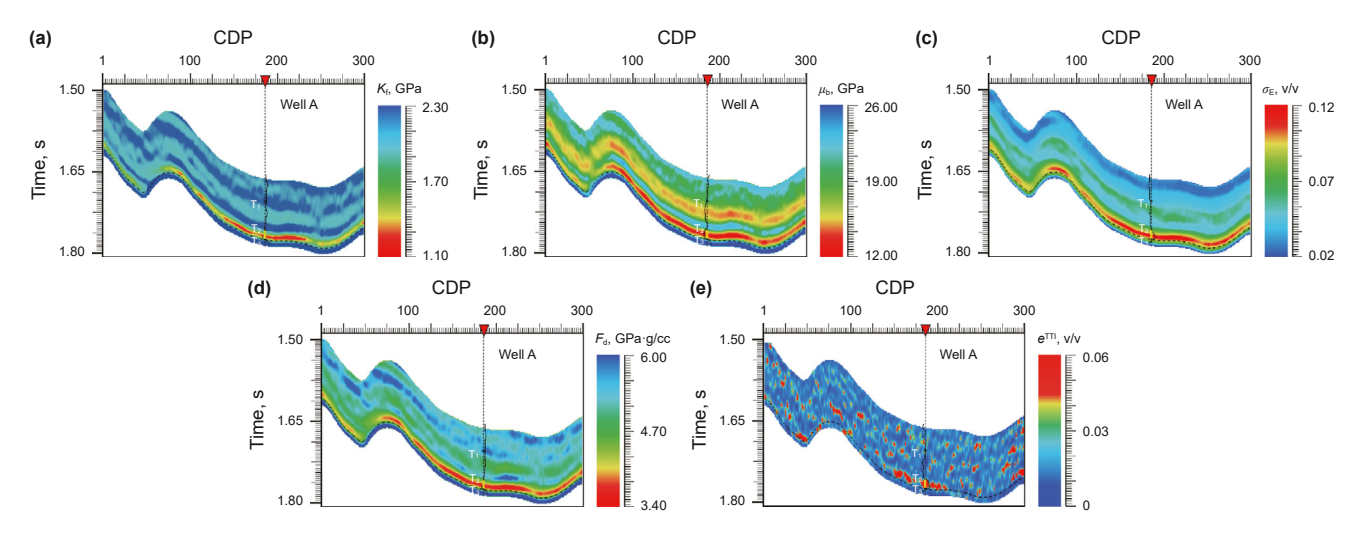


Fig. 22. 2D inversion results of elasticity and fracture parameters for an arbitrary survey line, where (a) fluid bulk modulus, (b) shear modulus, (c) effective stress parameter, (d) F_d parameter, and (e) tilted fracture density.

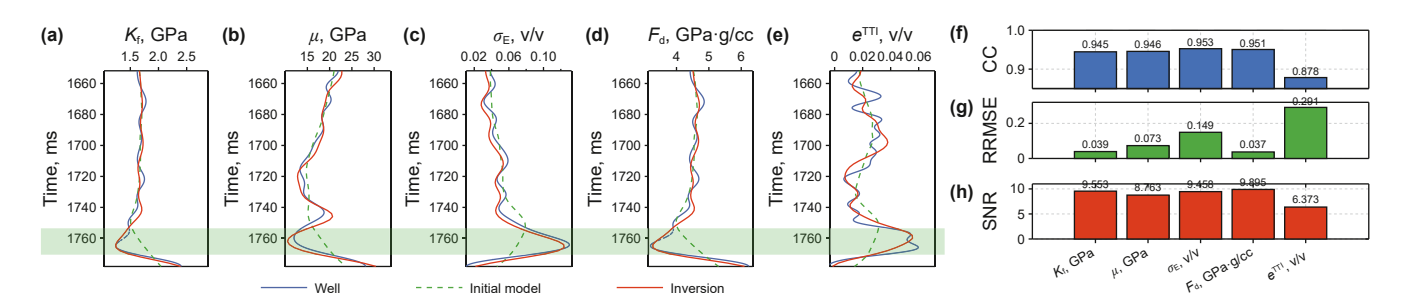


Fig. 23. Comparison of Well A location logging curves, where (a) fluid bulk modulus, (b) shear modulus, (c) effective stress parameter, (d) F_d parameter, and (e) tilted fracture density, (f) CC, (g) RRMSE, (h) SNR.

values in the reservoir section, indicating that the shale rock around Well A is under lower vertical stress and may have higher pore pressure, which correlates positively with the conclusion on shale gas enrichment. The fracture density in Fig. 22(e) characterizes the development of natural fractures. Therefore, we can characterize the reservoir as processing low fluid bulk modulus in Fig. 22(a), low shear modulus in Fig. 22(b), high effective stress parameter in Fig. 22(c), and high fracture density in Fig. 22(e), which agree well with the logging curves in black. The effects of the inversion results for well A at trace of 187 are compared with the logging curves, as shown in Fig. 23(a)-(e). The red curves represent the inversion result curves at Well A, the green curves indicate the low-frequency initial models, the blue curves correspond to the logging curves, and the green rectangular background portion highlights the fractured reservoir. The fluid bulk modulus in Fig. 23(a), shear modulus in Fig. 23(b), effective stress parameter in Fig. 23(c), and F_d parameter in Fig. 23(d) aligns well with the corresponding logging curves. Specifically, the fracture density in Fig. 23(e) closely aligns with the logging curve, with a slightly inferior match compared to the isotropic parameters. The quantitative evaluation indexes CC, RRMSE, and SNR calculated based on Eqs. (68)-(70), are demonstrated in Fig. 23(f)–(h). The CCs of the isotropic parameters are higher than 0.94, and the CC of the tilted fracture density is slightly lower at 0.878. The RRMSEs remain below 0.30, and the SNRs are above 6.37. To further predict the distribution of fluids, natural fractures, and effective stress parameter, we have performed the following 3D systematic seismic inversion, as displayed in Fig. 24(a)-(c).

The 3D work zone contains 230 Inlines and 270 Crosslines. The predicted slice results for fluid bulk modulus, effective stress parameter, and fracture density are exhibited along the bottom of the Wufeng Formation. As indicated by the dashed ellipse and arrow near Well A in Fig. 24(a)-(c), the low fluid bulk modulus suggests a high potential for containing shale gas in Fig. 24(a). The higher effective stress parameter in Fig. 24(b) indicates lower vertical effective stress σ_V with higher porosity or high pore pressure, which is consistent with the above conclusion of enriched shale gas in Fig. 24(a). The high fracture density in Fig. 24(c) indicates that the natural fracture development around the Well A, which can provide storage and transportation space in fractured gas-bearing shale reservoirs. Additionally, they have the native ability to connect with artificial fracture and form complex fracture networks more efficiently during the hydraulic fracturing process. Thus, the block marked by the white dotted line is more beneficial to the hydraulic compressibility of shale. Furthermore, the geologic fault F₁ as a permeability channel exhibited more stratum brine, and the fluid bulk modulus detected markedly high-value anomalies in Fig. 24(a), which is unfavorable for fracturing and well construction. As a consequence of tectonic activity, the rocks were broken, forming fracture zones, the stresses have been released, and high vertical effective stress is concentrated at the base of the fault related to the low effective stress parameter in Fig. 24(b) and the tectonic natural fracture induced by the faulting has resulted in higher fracture density along the strike of fault F₁ in Fig. 24(c). Generally, with the formation of fault F₁, tectonically-induced natural fractures have been generated to form fracture zones

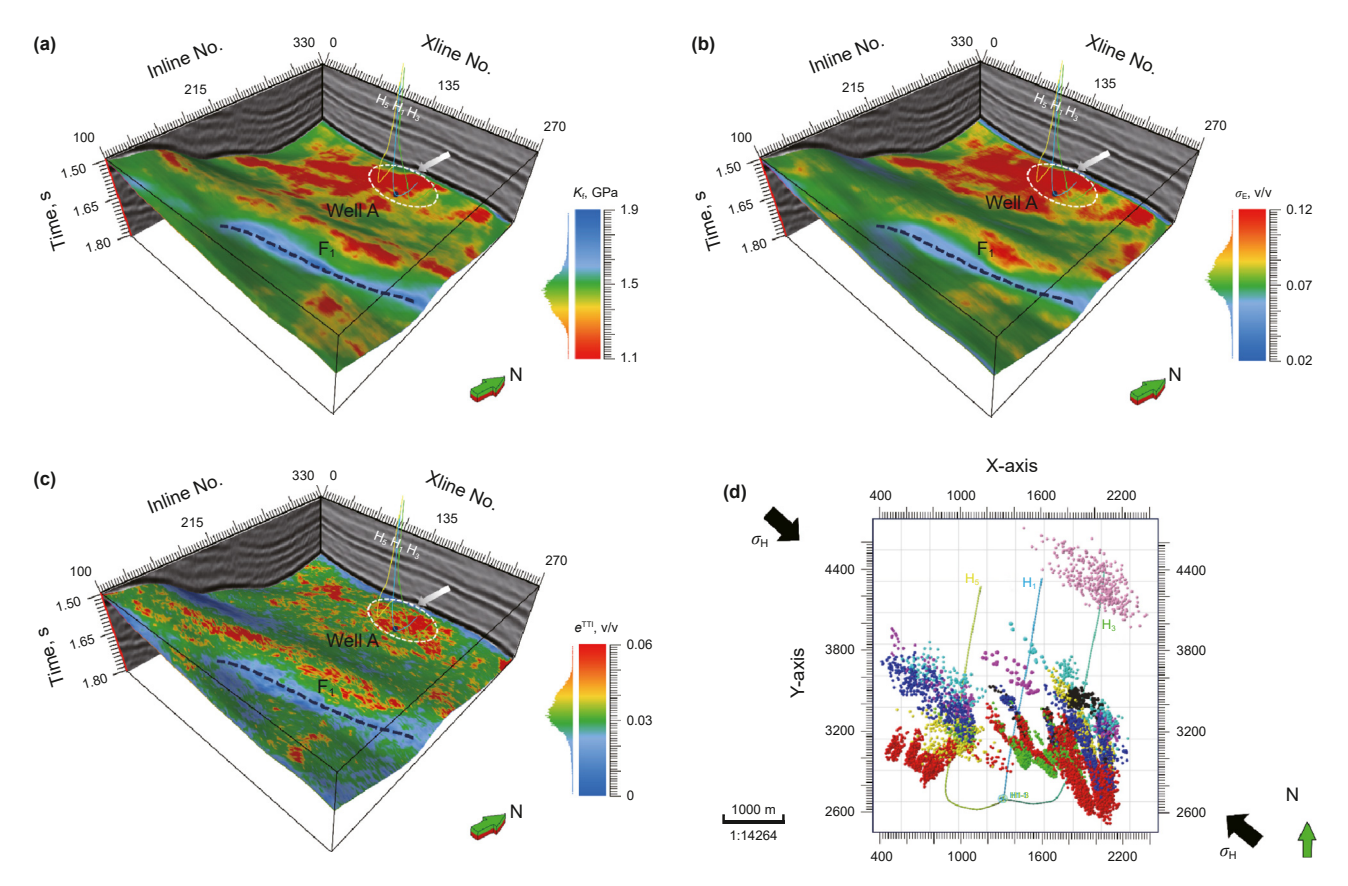


Fig. 24. 3D inversion results for elasticity and fracture parameters. (a) Fluid bulk modulus, (b) effective stress parameter, (c) tilted fracture density, and (d) microseismic event detection.

along it, of which the hanging wall (north of F_1) has more widely distributed fractures, and the footwall (south of F_1) has fewer fractures confined to its vicinity.

Eventually, three horizontal wells, etc., Well H₁, H₃, and H₅, are oriented orthogonally to the direction of the maximum horizontal principal stress for hydraulic fracturing and microseismic event detection, as shown in Fig. 24(d). The different colored dots represent the microseismic events detected at different times, corresponding to the dashed circles in Fig. 24(a)–(c). It is evident from the microseismic data that significant rock fragmentation and hydraulic fracture formation occur along the direction of the maximum horizontal principal stress σ_H , with the rock exhibiting notable brittleness. This hydraulic fracturing is expected to promote surrounding natural fracture activation connectivity, facilitating shale reservoir development and modification. Furthermore, the microseismic events are also potentially attributed to the activation and connectivity of natural fracture at this location by the hydraulic fracturing fluid (Li et al., 2023; Yu et al., 2023), thereby validating the accuracy and reliability of the predictive results in the gas-bearing fractured shale reservoirs.

4. Conclusions

In this study, we develop a simultaneous seismic inversion method for fluid bulk modulus, effective stress parameter, and fracture density in TTI media. It enables the detection of shale gas, stress distribution, and tilted fractures, providing a reasonable basis for effectively exploiting shale gas.

- (1) The novel PP-wave reflection coefficient equation is derived by linearizing the stiffness perturbations of the TTI medium, which has realized the direct seismic inversion of the fluid bulk modulus, effective stress parameter, and fracture density. High-quality shale gas reservoirs are characterized by the low fluid bulk modulus, high effective stress parameter, and high fracture density.
- (2) The accuracy of the proposed equation is validated using an anisotropic two-layer model, demonstrating its reliability across various azimuths, incidence angles, and fracture inclination angles. Seismic inversion method based on L_P quasi-norm sparsity constraint is proven to effectively decouple the fluid bulk modulus, effective stress parameter, and fracture density through three sets of tests. Moreover, incorporating azimuthal amplitude difference seismic data enhances the stability and accuracy of fracture density inversion.
- (3) The method is applied to a gas-bearing shale reservoir in the Longmaxi-Wufeng Formation in the Sichuan Basin, China. The lower fluid bulk modulus can directly characterize the shale-gas enrichment situation, the higher effective stress parameter may indicate the higher porosity, and the fracture density characterizes the natural tilted fracture development scale and extension characteristics. The geological structures, logging interpretation, and microseismic events justify the inversion results.

In conclusion, the direct seismic inversion method of fluid bulk modulus, effective stress parameter, and fracture density achieved in this paper can provide accurate and reliable support for reservoir prediction and shale gas exploitation.

CRediT authorship contribution statement

Yun Zhao: Writing — original draft, Methodology, Investigation, Formal analysis. **Chun-Lan Xie:** Visualization, Validation, Conceptualization. **Bo Li:** Software, Resources, Funding acquisition. **Chen-Long Li:** Visualization, Supervision, Investigation. **Xiao Pan:** Funding acquisition, Validation. **Xi-Yan Zhou:** Funding acquisition, Visualization.

Declaration of competing interest

The authors declare that they have no known competing financial interests or personal relationships that could have appeared to influence the work reported in this paper.

Acknowledgments

This study was financially supported by the Natural Science Foundation of Sichuan Province (Grant Nos. 2023NSFSC0767 and 2024NSFSC0809), the China Postdoctoral Science Foundation (Grant No. 2024MF750281), and the Postdoctoral Fellowship Program of CPSF (Grant No. GZC20230326). The authors who contributed to the writing and revision of this article are greatly appreciated. The authors also thank the editorial board and the reviewers for their valuable and constructive suggestions.

Appendix A

Based on the Bond transform theory (Winterstein, 1990) for parallel fractures incorporates the fracture inclination angle, the stiffness matrix of anisotropic TTI saturated rock can be given (Ma et al., 2022, 2023) as

$$\begin{split} C_{11}^{sat} = & \, 4\mu_b \Big(\delta_T^{dry} - g_d \delta_N^{dry} \Big) cos^4 \, \, \zeta + 4\mu_b \Big(\delta_N^{dry} - \delta_T^{dry} \Big) cos^2 \, \, \zeta \\ & + M_d \Big(1 - \delta_N^{dry} \Big) + G_n \Big(\phi_p \Big) K_f \end{split} \tag{A-1}$$

 $C_{12}^{\text{sat}} = 2\mu_{\text{b}}\chi_{\text{d}}\delta_{\text{N}}^{\text{dry}}\cos^{2}\zeta + \lambda_{\text{d}}\left(1 - \delta_{\text{N}}^{\text{dry}}\right) + G_{\text{n}}\left(\phi_{\text{p}}\right)K_{\text{f}} \tag{A-2}$

$$\begin{split} C_{13}^{sat} = & \, 4\mu_b \Big(g_d \delta_N^{dry} - \delta_T^{dry}\Big) cos^4 \, \, \zeta + 4\mu_b \Big(\delta_T^{dry} - g_d \delta_N^{dry}\Big) cos^2 \, \, \zeta \\ & + \lambda_d \Big(1 - \delta_N^{dry}\Big) + G_n \Big(\phi_p\Big) K_f \end{split}$$

(A-3)

$$C_{15}^{\text{sat}} = \left[2\mu_{\text{b}}\left(\delta_{\text{T}}^{\text{dry}} - g_{\text{d}}\delta_{\text{N}}^{\text{dry}}\right)\cos^{2}\zeta + \mu_{\text{b}}\left(\delta_{\text{N}}^{\text{dry}} - \delta_{\text{T}}^{\text{dry}}\right)\right]\sin 2\zeta \tag{A-4}$$

$$C_{22}^{\text{sat}} = M_{\text{d}} \left[1 - \chi_{\text{d}}^{2} \delta_{\text{N}}^{\text{dry}} \right] + G_{\text{n}} \left(\phi_{\text{p}} \right) K_{\text{f}} \tag{A-5}$$

$$C_{23}^{\text{sat}} = -2\lambda_{\text{d}}g_{\text{d}}\delta_{\text{N}}^{\text{dry}}\cos^{2}\zeta + \lambda_{\text{d}}\left(1 - \chi_{\text{d}}\delta_{\text{N}}^{\text{dry}}\right) + G_{\text{n}}\left(\phi_{\text{p}}\right)K_{\text{f}} \tag{A-6}$$

$$C_{25}^{\text{sat}} = g_{\text{d}} \lambda_{\text{d}} \delta_{\text{N}}^{\text{dry}} \sin 2\zeta \tag{A-7}$$

$$\begin{split} C_{33}^{sat} &= 4\mu_b \Big(\delta_T^{dry} - g_d \delta_N^{dry} \Big) cos^4 \ \zeta - 4\mu_b \Big(\chi_d \delta_N^{dry} + \delta_T^{dry} \Big) cos^2 \ \zeta \\ &\quad + M_d \Big[1 - (\chi_d)^2 \delta_N^{dry} \Big] + G_n \Big(\phi_p \Big) K_f \end{split} \tag{A-8}$$

$$\begin{split} C_{35}^{sat} = \left[2\mu_{b} \Big(g_{d} \delta_{N}^{dry} - \delta_{T}^{dry} \Big) cos^{2} \; \zeta + \mu_{b} \Big(\chi_{d} \delta_{N}^{dry} + \delta_{T}^{dry} \Big) \right] sin \; 2\zeta \end{split} \tag{A-9}$$

$$C_{44}^{\text{sat}} = -\mu_{\text{b}} \delta_{\text{T}}^{\text{dry}} \cos^2 \zeta + \mu_{\text{b}} \tag{A-10}$$

$$C_{46}^{\text{sat}} = \mu_b \delta_{\text{T}}^{\text{dry}} \sin \zeta \cos \zeta \tag{A-11}$$

$$\begin{split} C_{55}^{sat} &= 4\mu_b \Big(g_d \delta_N^{dry} - \delta_T^{dry}\Big) cos^4 \; \zeta - 4\mu_b \Big(g_d \delta_N^{dry} - \delta_T^{dry}\Big) cos^2 \; \zeta \\ &\quad + \mu_b \Big(1 - \delta_T^{dry}\Big) \end{split} \tag{A-12}$$

 $C_{66}^{\text{sat}} = \mu_{\text{b}} \delta_{\text{T}}^{\text{dry}} \cos^2 \zeta + \mu_{\text{b}} \left(1 - \delta_{\text{T}}^{\text{dry}} \right) \tag{A-13}$

where C_{ii}^{sat} is the stiffness coefficient of saturated anisotropic rock.

Then, the Born scattering theory (Shaw and Sen, 2004, 2006) and first-order perturbation are used to linear the PP-wave reflection coefficient based on the perturbation of the stiffness coefficient with scattering function, which is given as

$$S(\mathbf{r_0}) = \Delta \rho \left[t_i t_i' \right] \Big|_{\mathbf{r} = \mathbf{r_0}} + \Delta \mathbf{C}_{mn} \left[t_i' s_j' t_k s_l \right] \Big|_{\mathbf{r} = \mathbf{r_0}}$$
(A-14)

in which

$$\begin{split} \xi^{\text{PP}} &= \cos^2\theta - \sin^2\theta = \cos2\theta = \Delta\rho\xi^{\text{PP}} + \Delta C_{ij}^{\text{sat}} \xi_{ij}^{\text{PP}} = \Delta\rho\cos2\theta \\ &+ \Delta C_{11}^{\text{sat}} \xi_{11}^{\text{PP}} + \Delta C_{22}^{\text{sat}} \xi_{22}^{\text{PP}} + \Delta C_{33}^{\text{sat}} \xi_{33}^{\text{PP}} + \Delta C_{44}^{\text{sat}} \xi_{44}^{\text{PP}} + \Delta C_{55}^{\text{sat}} \xi_{55}^{\text{PP}} \\ &+ \Delta C_{66}^{\text{sat}} \xi_{66}^{\text{PP}} + 2\Delta C_{12}^{\text{sat}} \xi_{12}^{\text{PP}} + 2\Delta C_{13}^{\text{sat}} \xi_{13}^{\text{PP}} + 2\Delta C_{23}^{\text{sat}} \xi_{23}^{\text{PP}} \end{split} \tag{A-15}$$

$$\xi_{11}^{PP} = \sin^4\theta \cos^4\Phi / \left(\alpha^{sat}\right)^2 \tag{A-16}$$

$$\xi_{22}^{PP} = \sin^4 \theta \sin^4 \Phi / \left(\alpha^{\text{sat}}\right)^2 \tag{A-17}$$

$$\xi_{33}^{PP} = \cos^4 \theta / (\alpha^{\text{sat}})^2 \tag{A-18}$$

$$\xi_{44}^{PP} = -4\sin^2\theta\cos^2\theta\sin^2\Phi/\left(\alpha^{sat}\right)^2 \tag{A-19}$$

$$\xi_{55}^{PP} = -4\sin^2\theta\cos^2\theta\cos^2\Phi/\left(\alpha^{\text{sat}}\right)^2 \tag{A-20}$$

$$\xi_{66}^{\text{PP}} = 4 \sin^4 \theta \sin^2 \Phi \cos^2 \Phi / (\alpha^{\text{sat}})^2$$
 (A-21)

$$\xi_{12}^{PP} = \sin^4 \theta \sin^2 \Phi \cos^2 \Phi / (\alpha^{sat})^2, \xi_{21}^{PP} = \xi_{12}^{PP}$$
 (A-22)

$$\xi_{13}^{PP} = \sin^2 \theta \cos^2 \theta \cos^2 \Phi / (\alpha^{sat})^2, \xi_{31}^{PP} = \xi_{13}^{PP}$$
 (A-23)

$$\xi_{23}^{PP} = \sin^2 \theta \cos^2 \theta \sin^2 \Phi / (\alpha^{sat})^2, \xi_{32}^{PP} = \xi_{23}^{PP}$$
 (A-24)

where $\Delta C_{ij}^{\text{sat}}$ and α^{sat} denote perturbation of the stiffness matrix and P-wave velocity in saturated rock, respectively.

References

- AL-Musaylh, M.S., Al-Daffaie, K., Prasad, R., 2021. Gas consumption demand forecasting with empirical wavelet transform based machine learning model: a case study. Int. J. Energy Res. 45 (5), 1–15. https://doi.org/10.1002/er.6788.
- Athy, L.F., 1930. Density, porosity, and compaction of sedimentary rocks. AAPG Bull. 14, 1–24. https://doi.org/10.1306/3D93289E-16B1-11D7-8645000102C1865D.
- Bakulin, A., Grechka, V., Tsankin, I., 2000a. Estimation of fracture parameters from reflection seismic data—Part I: HTI model due to a single fracture set. Geophysics 65 (6), 1708–2018. https://doi.org/10.1190/1.1444863.
- Bakulin, A., Grechka, V., Tsankin, I., 2000b. Estimation of fracture parameters from reflection seismic data—Part II: fractured models with orthorhombic symmetry. Geophysics 65 (6), 1708–2018. https://doi.org/10.1190/1.1444864.
- Bakulin, A., Grechka, V., Tsankin, I., 2000c. Estimation of fracture parameters from reflection seismic data—Part III: fractured models with monoclinic symmetry. Geophysics 65 (6), 1818–1830. https://doi.org/10.1190/1.1444865.
- Brown, R.J.S., Korringa, J., 1975. On the dependence of the elastic properties of a porous rock on the compressibility of the pore fluid. Geophysics 40 (4), 593–701. https://doi.org/10.1190/1.1440551.
- Chen, H.Z., Chen, T.S., Innanen, K.A., 2020a. Estimating tilted fracture weaknesses from azimuthal differences in seismic amplitude data. Geophysics 85 (3), 1MJ–Z13. https://doi.org/10.1190/geo2019-0344.1.
- Chen, H.Z., Li, J., Innanen, K.A., 2020b. Nonlinear inversion of seismic amplitude variation with offset for an effective stress parameter. Geophysics 85 (4), R299–R311. https://doi.org/10.1190/geo2019-0154.1. Chen, H.Z., Yin, X.Y., Qu, S.L., Zhang, G.Z., 2014. AVAZ inversion for fracture weakness
- Chen, H.Z., Yin, X.Y., Qu, S.L., Zhang, G.Z., 2014. AVAZ inversion for fracture weakness parameters based on the rock physics model. J. Geophys. Eng. 11 (6), 065007. https://doi.org/10.1088/1742-2132/11/6/065007.
- Chen, H.Z., Zhang, G.Z., Ji, Y.X., Yin, X.Y., 2017. Azimuthal seismic amplitude difference inversion for fracture weakness. Pure Appl. Geophys. 174 (1), 279–291. https://doi.org/10.1007/s00024-016-1377-x.
- Dutta, N.C., 2002. Geopressure prediction using seismic data: current status and the road ahead. Geophysics 67 (6), 2012–2041. https://doi.org/10.1190/1.1527101.
- Ding, P.B., Wang, D., Di, G.D., Li, X.Y., 2019. Investigation of the effects of fracture orientation and saturation on the vp/vs ratio and their implications. Rock Mech. Rock Eng. 52 (9), 3293—3304. https://dio.org/10.1007/s00603-019-01770-3.
- Flemings, P.B., Stump, B.B., Finkbeiner, T., Zoback, M., 2002. Flow focusing in over-pressured sandstones: theory, observations, and applications. Am. J. Sci. 302 (10), 827–855. https://doi.org/10.2475/ajs.302.10.827.
- Goodway, B., Chen, T., Downton, J., 1997. Improved AVO fluid detection and lithology discrimination using Lamé petrophysical parameters. "λρ", "μρ", "λμ fluid stack", from P and S inversions. SEG. Tech. Program. Expand. Abstr. https://doi.org/10.1190/1.1885795.
- Gray, F.D., Anderson, P., Logel, J., Delbecq, F., Schmidt, D., 2010. Estimating In-situ, Anisotropic, Principal Stresses from 3D Seismic. In: 72nd EAGE Conference and Exhibition incorporating SPE EUROPEC 2010. https://doi.org/10.3997/2214-4609.201400910
- Gray, F.D., Anderson, P., Logel, J., Delbecq, F., Schmidt, D., Schmid, R., 2012. Estimation of stress and geomechanical properties using 3D seismic data. First Break 30 (3). https://doi.org/10.3997/1365-2397.2011042.
- Guo, Z.Q., Nie, N.F., Liu, C., 2022a. Fracture characterization based on improved seismic amplitude variation with azimuth inversion in tight gas sandstones, Ordos Basin. China. Mar. Petrol. Geol. 146, 105941. https://doi.org/10.1007/ s10712-022-09726-z.
- Guo, Z.Q., Zhang, X.D., Liu, C., Liu, X.W., Liu, Y.W., 2022b. Hydrocarbon identification and bedding fracture detection in shale gas reservoirs based on a novel seismic dispersion attribute inversion method. Surv. Geophys. 43, 1793–1816. https:// doi.org/10.1007/s10712-022-09726-z.
- Guo, Z.Q., Zhang, X.D., Liu, C., 2022c. An improved scheme of azimuthally anisotropic seismic inversion for fracture prediction in volcanic gas reservoirs. IEEE Trans. Geosci. Remote Sens. 60, 5917312. https://doi.org/10.1109/TGRS.2022.3186426.
- Han, D., Batzle, M., 2003. Gain function and hydrocarbon indicators: 73rd annual international meeting. SEG, Expanded Abstracts 1695–1698. https://doi.org/ 10.1190/1.1817633.
- Hubbert, M.K., Willis, D.G., 1957. Mechanics of hydraulic fracturing. OR Trans. 210 (1), 153–168. https://doi.org/10.2118/686-G.
- Iftikhar, B., Alih, S.C., Vafaei, M., Elkotb, M.A., Shutaywi, M., Javed, M.F., Deebani, W., Khan, M.I., Aslam, F., 2022. Predictive modeling of compressive strength of sustainable rice husk ash concrete: ensemble learner optimization and comparison. J. Clean. Prod. 348, 131258. https://doi.org/10.1016/j.jclepro.2022.131285.
- Kauerauf, A.I., Hantschel, T., 2009. Fundamentals of basin and petroleum systems

- modeling. https://link.springer.com/book/10.1007/978-3-540-72318-9.
- Li, D., Zheng, J., Peng, S., Yang, R., Meng, L., Shi, W., 2023. Hydraulic fracturing-induced microseismicity controlled by rock brittleness and natural fractures in Tongren, Guizhou, China. Interpretation 11, T745–T755. https://doi.org/10.1190/INT-2022-0126.1.
- Li, L., Zhang, G.Z., Pan, X.P., Guo, X.L., Zhang, J.J., Zhou, Y., Lin, Y., 2022a. Anisotropic poroelasticity and AVAZ inversion for in situ stress estimate in fractured shalegas reservoirs. IEEE Trans. Geosci 60, 1–13. https://doi.org/10.1109/TGRS.2022.3146258.
- Li, L., Guo, Y.M., Zhang, G.Z., Pan, X.P., Zhang, J.J., Lin, Y., 2022b. Seismic characterization of in situ stress in orthorhombic shale reservoirs using anisotropic extended elastic impedance inversion. Geophysics 87 (6), M259—M274. https://doi.org/10.1190/geo2021-0807.1.
- Li, L., Zhang, G.Z., Pan, X.P., Liu, J.X., 2021. Estimating effective stress parameter and fracture parameters in shale-gas fractured reservoirs using azimuthal fourier coefficients. Surv. Geophys. 42 (6), 1377–1400. https://doi.org/10.1007/s10712-021-09671-3
- Lin, K., Zhang, B., Zhang, J.J., Fang, H.J., Xi, K.F., Li, Z., 2022. Predicting the azimuth of natural fractures and in situ horizontal stress: a case study from the Sichuan Basin, China. Geophysics 87 (1), B9–B22. https://doi.org/10.1190/geo2020-08291
- Long, H., Flemings, P.B., Germaine, J.T., Saffer, D.M., 2011. Consolidation and overpressure near the seafloor in the ursa basin, deepwater Gulf of Mexico. Earth Planet Sci. Lett. 305 (1), 11–20. https://doi.org/10.1016/j.epsl.2011.02.007.
- Ma, N., Yin, X.Y., Sun, C.Y., Zong, Z.Y., 2017. The in-situ stress seismic prediction method based on the theory of orthorhombic anisotropic media. Chin. J. Geophys. 60 (12), 4766–4775. http://en.dzkx.org/article/doi/10.6038/cjg20171218 (in Chinese).
- Ma, N., Yin, X.Y., Sun, C.Y., Zong, Z.Y., 2018. Inversion for crustal stress based on azimuthal seismic data. Chin. J. Geophys. 61 (2), 697–706. http://en.dzkx.org/ article/doi/10.6038/cjg2018L0183 (in Chinese).
- Mavko, G., Mukerji, T., Dvorkin, J., 2009. The Rock Physics Handbook-Tools for Seismic Analysis of Porous Media, second ed. Cambridge University Press, New York. https://doi.org/10.1017/CBO9780511626753.
- Ma, Z.Q., Yin, X.Y., Li, K., Tan, Y.Y., 2022. Fourier coefficients variation with angle for fracture detection and fluid discrimination in tilted transversely isotropic media. Surv. Geophys. 43 (3), 1–39. https://doi.org/10.1007/s10712-022-09704-5.
 Ma, Z.Q., Yin, X.Y., Zong, Z.Y., Tan, Y.Y., Ji, L.X., Yang, Z.F., Yan, X.F., 2023. Sequential
- Ma, Z.Q., Yin, X.Y., Zong, Z.Y., Tan, Y.Y., Ji, L.X., Yang, Z.F., Yan, X.F., 2023. Sequential Bayesian seismic inversion for fracture parameters and fluid indicator in tilted transversely isotropic media. Geophysics 88 (3), R355—R371. https://doi.org/ 10.1190/geo2022-0439.1.
- Nakamura, K., Kanatake, T., Inoue, M., Yamashita, A., 1997. Gold-silver-palladium alloys (20%) for dental casting. DE. J. Dent. Eng. (43), 1–13.
- Nikolaevskiy, V.N., Economides, M.J., 2000. Near-well state of stress and induced rock damage. Proc. - SPE Symp. Form. Damage Control 71–80. https://doi.org/ 10.2118/58716-MS.
- Pan, X.P., Zhang, D.Z., Zhang, P.F., Zhang, P.F., Zhang, G.Z., Cui, Y., Liu, J.X., 2020a. A coupled anisotropic fluid indicator for seismic characterization of tight gasbearing fractured reservoirs. J. Nat. Gas Sci. Eng. 83, 103552. https://doi.org/10.1016/j.jngse.2020.103552.
- Pan, X.P., Li, L., Zhou, S.X., Zhang, G.Z., Liu, J.X., 2020b. Azimuthal amplitude variation with offset parameterization and inversion for fracture weaknesses in tilted transversely isotropic media. Geophysics 86 (1), C1–C18. https://doi.org/10.1190/geo2019-0215.1.
- Pan, X.P., Liu, J.X., 2024. Stress dependent PP-wave refection coefficient for Fourier coefficients based seismic inversion in horizontally stressed vertical transversely isotropic media. Surv. Geophys. https://doi.org/10.1007/s10712-024-09841-z.
- Pan, X.P., Zhang, G.Z., Yin, X.Y., 2018a. Azimuthally pre-stack seismic inversion for orthorhombic anisotropy driven by rock physics. Sci. China Earth Sci. 61 (4), 425–440. https://doi.org/10.1007/s11430-017-9124-6.
- Pan, X.P., Zhang, G.Z., Yin, X.Y., 2018b. Azimuthal seismic amplitude variation with offset and azimuth inversion in weakly anisotropic media with orthorhombic symmetry. Surv. Geophys. 39, 99–123. https://doi.org/10.1007/s10712-017-9434-2.
- Pan, X.P., Zhang, G.Z., Yin, X.Y., 2017. Azimuthally anisotropic elastic impedance inversion for fluid indicator driven by rock physics. Geophysics 82 (6), 1ND–Z46. https://doi.org/10.1190/geo2017-0191.1.
- Pšenčík, I., Martinš, J.L., 2001. Properties of weak contrast PP reflection/transmission coefficients for weakly anisotropic elastic media. Studia Geophys. Geod. 45, 176–199. https://doi.org/10.1023/A:1021868328668.
- Qin, Z.Y., Wen, X.T., Zhou, D.Y., Li, B., Chen, J.Y., 2022. Inversion method of elastic and fracture parameters of shale reservoir with a set of inclined fractures. IEEE Trans. Geosci. 60, 1–13. https://doi.org/10.1109/TGRS.2021.3138750.
- Rubey, W.W., Hubbert, K.M., 1959. Role of fluid pressure in mechanics of overthrust faulting: II. Overthrust belt in geosynclinal area of western Wyoming in light of fluid-pressure hypothesis. Geol. Soc. Am. Bull. 70 (2), 167–206. https://doi.org/ 10.1130/0016-7606(1959)70[167:ROFPIM]2.0.CO;2.
- Ruger, A., 1998. Variation of P-wave reflectivity with offset and azimuth in anisotropic media. Geophysics 63 (3), 935–947. https://doi.org/10.1190/1.1444405.
- Russell, B.H., Hampson, D.P., Gray, D., 2011. Linearized AVO and poroelasticity. Geophysics 76 (3), 1MJ–Z74. https://doi.org/10.1190/1.3555082.

- Sayers, C.M., Dean, S., 2001. Azimuth-dependent AVO in reservoirs containing non-orthogonal fracture sets. Geophys. Prospect. 49 (1), 100–106. https://doi.org/10.1046/j.1365-2478.2001.00236.x.
- Schoenberg, M., Sayers, C.M., 1995. Seismic anisotropy of fractured rock. Geophysics 60 (1), 204. https://doi.org/10.1190/1.1443748.
- Schoenberg, M., Douma, J., 1988. Elastic wave propagation in media with parallel fractures and aligned cracks. Geophys. Prospect. 36 (6), 571–590. https://doi.org/10.1111/j.1365-2478.1988.tb02181.x.
- Seto, M., Nag, D.K., Vutukuri, V.S., 1999. In-situ rock stress measurement from rock cores using the acoustic emission method and deformation rate analysis. Geotech 17 (3–4), 241–266. https://doi.org/10.1023/A:1008981727366.
- Shaw, R.K., Sen, M.K., 2004. Born integral, stationary phase and linearized reflection coefficients in weak anisotropic media. Geophys. J. Int. 158 (1), 225–238. https://doi.org/10.1111/j.1365-246X.2004.02283.x.
- Shaw, R.K., Sen, M.K., 2006. Use of AVOA data to estimate fluid indicator in a vertically fractured medium. Geophysics 71 (3), C15–C24. https://doi.org/ 10.1190/1.2194896.
- Thomsen, L., 1986. Weak elastic anisotropy. Geophysics 51 (10), 1879–2018. https://doi.org/10.1190/1.1442051.
- Uyanik, O., 2010. Compressional and shear-wave velocity measurements in unconsolidated top-soil and comparison of the results. Int. J. Phys. Sci. 5 (7), 1034–1039. https://dio.org/10.1142/S0218127410027064.
- Winterstein, D.F., 1990. Velocity anisotropy terminology for Geophysicsts. Geophysics 55 (8), 1070–1088. https://doi.org/10.1190/1.1442919.
- Wen, X.T., Zhao, Y., Xie, C.L., Li, C.L., 2024. Direct seismic inversion of a novel brittleness index based on petrophysical modeling in shale reservoirs. IEEE Trans. Geosci. Rem. Sens. 62, 5923115. https://doi.org/10.1109/TGRS.2024.3436896.
- Xue, J., Gu, H.M., Cai, C.G., 2017. Model-based amplitude versus offset and azimuth

- inversion for estimating fracture parameters and fluid content. Geophysics 82 (2), M1–M17. https://doi.org/10.1190/geo2016-0196.1.
- Yin, X.Y., Ma, N., Ma, Z., Zong, Z.Y., 2018. Review of in-situ stress prediction technology. J. Geophys. Res. 57 (4), 488–504. https://doi.org/10.3969/j.issn.1000-1441.2018.04.001.
- Yin, X.Y., Zhang, S.X., 2014. Bayesian inversion for effective pore-fluid bulk modulus based on fluid-matrix decoupled amplitude variation with offset approximation. Geophysics 79 (5), R221–R232. https://doi.org/10.1190/geo2013-0372.1.
- Yu, C.P., Zhu, Y.L., Shapiro, S., 2023. Seismic anisotropy estimation using a downhole microseismic data set in a shale gas reservoir. Energies 16 (23), 7857. https:// doi.org/10.3390/en16237857.
- Zhang, G.Z., Li, L., Pan, H.X., Li, H.X., Liu, J.Z., Han, L., 2020. Azimuthal Fourier coefficient inversion for horizontal and vertical fracture characterization in weakly orthorhombic media. Geophysics 85 (6), 199–214. https://doi.org/10.1190/geo2019-0797.1.
- Zhang, G.Z., Chen, J.J., Chen, H.Z., Ma, Z.G., Li, C.C., Yin, X.Y., 2015. Prediction for insitu formation stress of shale based on rock physics equivalent model: chin. J. Geophys. 58 (6), 2112–2122 (in Chinese). http://en.dzkx.org/article/doi/10.6038/cjg20150625.
- Zhang, Y.S., Zhang, J.C., Yuan, B., Yin, S.X., 2018. In-situ stresses controlling hydraulic fracture propagation and fracture breakdown pressure. Petrol. Sci. Eng. 164, 164–173. https://doi.org/10.1016/j.petrol.2018.01.050.
- Zhao, L., Lin, L., Wen, X.T., Zhang, Y.Q., 2023. The 3-D global prestack seismic inversion in the time—frequency mixed domain. IEEE Trans. Geosci 61, 1–14. https://doi.org/10.1109/TGRS.2023.3282250.
- Zhao, Y., Wen, X.T., Li, C.L., Liu, Y., Xie, C.L., 2024. Systematic prediction of the gas content, fractures, and brittleness in fractured shale reservoirs with TTI medium. Pet. Sci. 21 (5), 3202–3221. https://doi.org/10.1016/j.petsci.2024.04.015.